

**WIND TUNNEL AND FLIGHT TESTING OF  
ACTIVE FLOW CONTROL ON A UAV**

A Thesis

by

YOGESH BABBAR

Submitted to the Office of Graduate Studies of  
Texas A&M University  
in partial fulfillment of the requirements for the degree of

MASTER OF SCIENCE

May 2010

Major Subject: Aerospace Engineering

**WIND TUNNEL AND FLIGHT TESTING OF  
ACTIVE FLOW CONTROL ON A UAV**

A Thesis

by

YOGESH BABBAR

Submitted to the Office of Graduate Studies of  
Texas A&M University  
in partial fulfillment of the requirements for the degree of

MASTER OF SCIENCE

Approved by:

Co-Chairs of Committee,	Othon K. Rediniotis
	John Valasek
Committee Member,	Mark T. Holtzapple
Head of Department,	Dimitris C. Lagoudas

May 2010

Major Subject: Aerospace Engineering

## ABSTRACT

Wind Tunnel and Flight Testing of Active Flow Control on a UAV. (May 2010)

Yogesh Babbar, B.E., Punjab Engineering College, Chandigarh, India

Co-Chairs of Advisory Committee: Dr. Othon K. Rediniotis  
Dr. John Valasek

Active flow control has been extensively explored in wind tunnel studies but successful in-flight implementation of an active flow control technology still remains a challenge. This thesis presents implementation of active flow control technology on-board a 33% scale Extra 330S ARF aircraft, wind tunnel studies and flight testing of fluidic actuators.

The design and construction of the pulsed blowing system for stall suppression (LE actuator) and continuous blowing system for roll control (TE actuator) and pitch control have been presented. Full scale wind tunnel testing in 7'×10' Oran W. Nicks low speed wind tunnel shows that the TE actuators are about 50% effective as the conventional ailerons. The LE actuator is found to be capable of suppressing stall from 12° to about 22°. Comparison of characteristics of active elevator and conventional elevator in 3'×4' low speed wind tunnel show that, the active elevator is as effective as the conventional elevator deflected at 5°.

Flight tests show that TE actuators are able to control the aircraft in flight in banked turns. The measured roll rates in-flight support the wind tunnel test findings.

## **DEDICATION**

I would like to dedicate this work to my parents, Mr. Om Prakash Babbar and Mrs. Bimla Babbar, whose unbounded faith in me always keeps me going.

## ACKNOWLEDGEMENTS

I would like to thank my committee chair, Dr. Rediniotis, my co-chair, Dr. Valasek, for their guidance and support throughout the course of this research. Suggestions on writing and presentation by my committee member, Dr. Holtzapple greatly helped me.

This project was funded by the Air Force Office of Scientific Research (AFoSR) and completed in collaboration with Aeroprobe Corporation. I would like to thank Matthew D. Zeiger and David Towery from Aeroprobe Corporation. As a part of the project team, I learned many things. Working on a real aircraft, and on a project that involves design, ground testing and flight testing of some novel systems was very fulfilling.

I would also like to extend my gratitude to Gaurav Agarwal who, along with Aeroprobe Corporation, designed many of the systems, and trained me to continue the project activity. Thanks also go to my colleagues, Shalom Johnson, and Andrew Beckett, for providing technical inputs and unlimited support.

Finally, I thank my department faculty and staff for making my time at Texas A&M University a great experience.

## NOMENCLATURE

AOA	Angle of Attack
UAV	Unmanned Aerial Vehicle
ARF	Almost Ready to Fly
FAA	Federal Aviation Administration
bhp	Brake Horse Power
rpm	Revolutions Per Minute
LE	Leading Edge
TE	Trailing Edge
LDA	Laser Doppler Anemometry
ABS	Acrylonitrile Butadiene Styrene
CAD	Computer Aided Design
L/D	Lift to Drag Ratio
$C_{PM}$	Coefficient of Pitching Moment
$C_{RM}$	Coefficient of Rolling Moment
B	Wingspan of Test Vehicle
W	Weight of Test Vehicle
L	Length of Test Vehicle
WL	Wing Loading of Test Vehicle
$C_{\mu}$	Coefficient of Jet Momentum
$F^+$	Reduced Frequency

$V_{jet}$	Velocity of Jet
$V_{\infty}$	Free-Stream Velocity
$f$	Frequency (Cycles per Second)
$h_{slot}$	Width of Jet Slot
$c$	Reference Chord
$LEC_{\mu}$	Coefficient of Jet Momentum of LE Actuator
$TEC_{\mu}$	Coefficient of Jet Momentum of TE Actuator
$ELC_{\mu}$	Coefficient of Jet Momentum of Active Elevator
$C_L$	Coefficient of Lift
$C_{L_{max}}$	Maximum Coefficient of Lift
$C_D$	Coefficient of Drag
OKID	Observer Kalman Identification

## TABLE OF CONTENTS

	Page
ABSTRACT .....	iii
DEDICATION .....	iv
ACKNOWLEDGEMENTS .....	v
NOMENCLATURE .....	vi
TABLE OF CONTENTS .....	viii
LIST OF FIGURES .....	x
LIST OF TABLES .....	xiv
 CHAPTER	
I      INTRODUCTION .....	1
Active flow control: overview .....	1
Gurney flap and jet flap .....	3
Uncertainty information .....	7
II     PROJECT SUMMARY .....	8
Previous work at Texas A&M University .....	8
Current work .....	9
III    TEST VEHICLE .....	12
IV    ROLL CONTROL AND STALL SUPPRESSION .....	14
Hardware design, construction and installation .....	14
Wind tunnel test setup .....	28
Configurations and test matrices .....	29
Plot Summary .....	34
Results .....	35
Summary of full scale wind tunnel test .....	45

CHAPTER	Page
V     PITCH CONTROL.....	46
Design and construction of active elevator .....	46
Elevator driving system.....	50
Active elevator performance .....	54
Wind tunnel test .....	56
Test matrix and information .....	62
Wind tunnel test results .....	63
VI    FLIGHT TESTING OF AIRCRAFT IN ROLL .....	69
Flight test procedure and location .....	69
Tested configurations .....	70
Comparison of roll rates and roll angles .....	72
Comparison of flight tests and wind tunnel results .....	74
VII   CONCLUSIONS .....	75
REFERENCES.....	77
VITA .....	82

## LIST OF FIGURES

	Page
Figure 1: A gurney flap[18] .....	3
Figure 2: Separation bubbles at the trailing edge of a conventional wing[18] .....	4
Figure 3: Effect of Gurney flap on separation bubbles[18] .....	4
Figure 4: Mean velocity vectors aft of gurney flap[22] .....	5
Figure 5: Time averaged streamlines for 4% Gurney flap at 0° AOA[22] .....	5
Figure 6: Vortex Shedding behind the Gurney Flap[22].....	6
Figure 7: 33% scale Hanger9 Extra 330S ARF.....	13
Figure 8: CAD model of the original wing .....	15
Figure 9: Modified Ribs 1-6 (Rib 1 is the wing tip rib) .....	15
Figure 10: CAD model of the active wing .....	16
Figure 11: Picture of the actual active wing with highlighted LE and TE actuators .....	16
Figure 12: CAD model of LE actuator embedded in the active wing .....	18
Figure 13: Leading edge fan module.....	18
Figure 14: Air inlet for LE fan module covered with aluminum mesh (underside view of the wing).....	19
Figure 15: Pulser module .....	20
Figure 16: Parts of pulser sub-assembly .....	21
Figure 17: Reduction gear for driving the pulser .....	21
Figure 18: CAD model of the TE actuator embedded in active wing .....	23
Figure 19: A view of wing tip rib (rib 1).....	24

	Page
Figure 20: TE actuator block fan module.....	24
Figure 21: CAD Model of the mouthpiece, full active wing in inset.....	25
Figure 22: Detailed view of jet flap deflected up.....	26
Figure 23: Micro servo for controlling jet flap .....	26
Figure 24: Heavy Wings under construction.....	27
Figure 25: 33% Extra 330S aircraft mounted in 7'×10' wind tunnel.....	28
Figure 26: Characteristics of aircraft in conventional configuration at 17 m/s.....	35
Figure 27: Comparison of characteristics of Basic, Reduced and Active Configurations with no deflections at 30 m/s.....	36
Figure 28: Comparison of $C_{RM}$ at $TEC\mu$ of 0.0024 .....	38
Figure 29: Comparison of $C_{RM}$ at $TEC\mu$ of 0.0075.....	39
Figure 30: Comparison of $C_{RM}$ for Active configuration at $TEC\mu = 0.0024$ and 0.0075 .....	40
Figure 31: Effect of pulsed blowing at $F + = 1$ on $CL$ and $LEC\mu = 0.0275$ at $TEC\mu = 0.0075$ .....	41
Figure 32: Effect of LE Pulser at $LEC\mu = 0.0275$ , $F + = 1$ on $CRM$ at $TEC\mu = 0.0075$ .....	42
Figure 33: Effect of LE Pulser at $LEC\mu = 0.0275$ , $F + = 1$ , both jet flaps deflected down, at $TEC\mu = 0.0075$ on $CL$ Vs. AOA.....	43
Figure 34: Conventional elevator.....	47
Figure 35: Active elevator.....	47

	Page
Figure 36: Detailed view and flow path for active elevator .....	49
Figure 37: Jet Flap Deflected upward .....	49
Figure 38: Airfoil profile comparison for conventional airfoil (top) and active airfoil (bottom).....	50
Figure 39: One of the fan modules for pitch control.....	51
Figure 40: CAD model of fuselage rear section of the aircraft .....	52
Figure 41: Identified sections for designing elevator duct .....	52
Figure 42: CAD model of elevator duct (section 3 detail in inset) .....	53
Figure 43: Picture of the Actual elevator Duct Parts .....	53
Figure 44: Numbered locations for measuring velocity profile .....	54
Figure 45: Jet velocity at location 6 .....	55
Figure 46: Velocity profile across 8 locations .....	56
Figure 47: 3D view of elevator mount apparatus .....	59
Figure 48: Modified test section.....	60
Figure 49: Front side view of the elevator mounted in test section .....	61
Figure 50: View of the elevator mounting setup with the center section of wall removed .....	61
Figure 51: $CL$ Vs AOA for baseline configurations of conventional and active elevator.....	63
Figure 52: $CL$ Vs AOA for –ve (down) deflections of Conventional and active elevator.....	64

## Page

Figure 53: <i>CL</i> Vs AOA for +ve (up) deflections of Conventional and active elevator....	65
Figure 54: Differential <i>CL</i> Vs. AOA for conventional and active elevators .....	65
Figure 55: <i>CD</i> Vs AOA for –ve (down) deflections of conventional and active elevator .....	67
Figure 56: Map of Riverside campus Runway .....	70
Figure 57: Roll Rate for Full Span Configuration.....	73
Figure 58: Roll Rate for Active Configuration .....	73

## LIST OF TABLES

	Page
Table 1: Specifications of 33% Extra 330S ARF.....	13
Table 2: Comparison of vehicle weight and wing loadings .....	28
Table 3: Characteristics of Oran W. Nicks low speed wind tunnel[31].....	29
Table 4: Configurations of full scale wind tunnel test .....	30
Table 5: Test Matrix for Basic configuration .....	31
Table 6: Test matrix for Reduced configuration .....	32
Table 7: Test Matrix for Active configuration .....	33
Table 8: Plot summary for wind tunnel tests.....	34
Table 9: Uncertainty in measured quantities in 7'×10' wind tunnel tests.....	44
Table 10: Specifications of conventional and active elevators .....	48
Table 11: Tests conducted in the wind tunnel.....	62
Table 12: Uncertainty information for elevator tests in 3'×4' wind tunnel .....	68
Table 13: Tested configurations .....	71
Table 14: Comparison of roll rates and roll angles from OKID analysis .....	72

# CHAPTER I

## INTRODUCTION

### ACTIVE FLOW CONTROL: OVERVIEW

Flow control is a fast growing multi-disciplinary science which aims at altering the natural flow path or state of the flow into a more desirable state or path[1]. Such an alteration can be made possible either actively or passively. Passive flow control techniques augment the boundary layer momentum through enhanced mixing or by introducing velocity fluctuations in the transverse direction to control the flow separation. Passive flow control methods include devices like vortex generators [2], distributed roughness, acoustic waves [3], self excited rods [4] riblets [5] etc. According to one of the classifications[1], steady suction and blowing techniques fall under passive modes of flow control. But in this work, any method that re-energizes the flow by either removing the low energy carrying fluid from the boundary layer or by increasing the boundary layer momentum, or involves moving elements, for example, steady blowing [6], steady suction [7] , moving surface elements [8], pulsed blowing [9], [10], oscillatory blowing/ suction [11], wall oscillations [12], vibrating ribbons [13] and synthetic jet actuators (SJA) [14-16] are classified as active flow control devices.

---

This thesis follows the style of AIAA Journal.

Flow control methods can also be classified based on their feedback as open-loop or closed-loop control systems. Closed-loop systems determine the value of one or more control parameters based on one or more system states.

The earlier demonstrations of the application of the active flow control technology to flight control have used compressed air supply [17], vibrating rods [4] etc. Compressed air based technology has difficulties in being used on a UAV platform because of constraints of payload, space and power available onboard a UAV. The vibrating rod method may have serious structural implications when implemented on a full scale aircraft. Application of net-zero mass flux actuators using piezoelectric transducers [15] have been practically demonstrated on an unmanned aerial vehicle. However, the aircraft has a limited operating range because of limited mass flow rates and frequency bandwidth and limited angle of attack regime in which the actuators are effective. The results suggest that a more global implementation approach is required for flight control that is effective throughout the angle of attack regime.

## GURNEY FLAP AND JET FLAP

Besides the use of active flow control to manipulate the boundary layer and achieve improved high angle of attack performance, current work also aims at replacing the conventional aileron with TE actuator. This actuator basically creates a sheet of air along the trailing edge which can be deflected with a small metal flap. The flap can also be used without the jet of air, as a gurney flap.

Figure 1 shows a sketch of a gurney flap. It is essentially a small plate attached or hinged at the trailing edge of the wing. The height generally varies from 0.5% to 3% of the chord length but the flap is intended to be inside the boundary layer. Liebeck [18] and Neuert [19] have discussed the aerodynamics and effects of gurney flaps in detail.

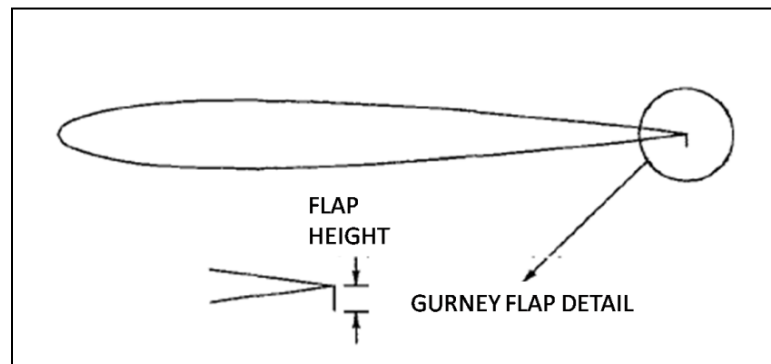


**Figure 1: A gurney flap[18]**

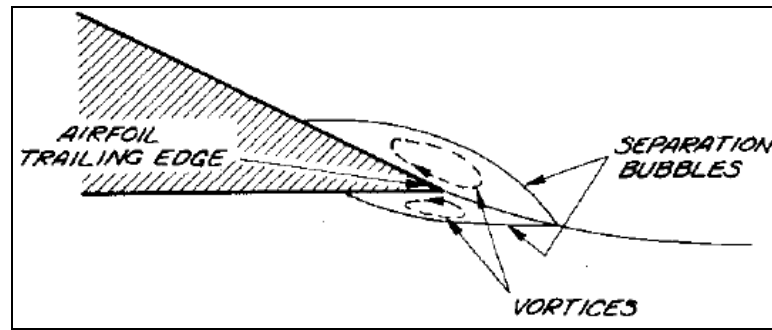


Figure 2: Separation bubbles at the trailing edge of a conventional wing[18]

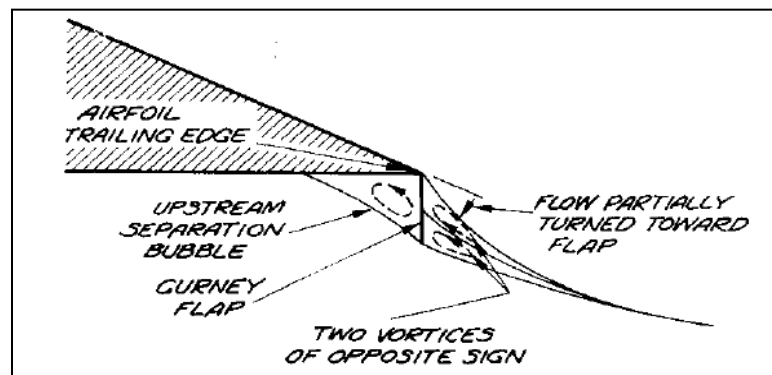


Figure 3: Effect of Gurney flap on separation bubbles[18]

Liebeck [18] has modeled the flow around the trailing edge of a conventional wing with two counter rotating vortices as shown in Figure 2. His results indicate an increase in the lift coefficient with a slight reduction in the drag with the use of a Gurney flap. The effect of gurney flap has been modeled as shown in Figure 3. Independent studies done by Myose [20-21] and Jeffrey [22] explain the phenomenon of high lift generated by Gurney flaps. Laser Doppler Anemometry (LDA) performed downstream of the flap [22] provides evidence of the extra flow turning that is caused by the flow aft of the flap.

This extra circulation translates into the extra lift. Figure 4 shows the mean velocity vectors and Figure 5 shows the time-averaged streamlines from LDA studies conducted by Jeffrey[22].

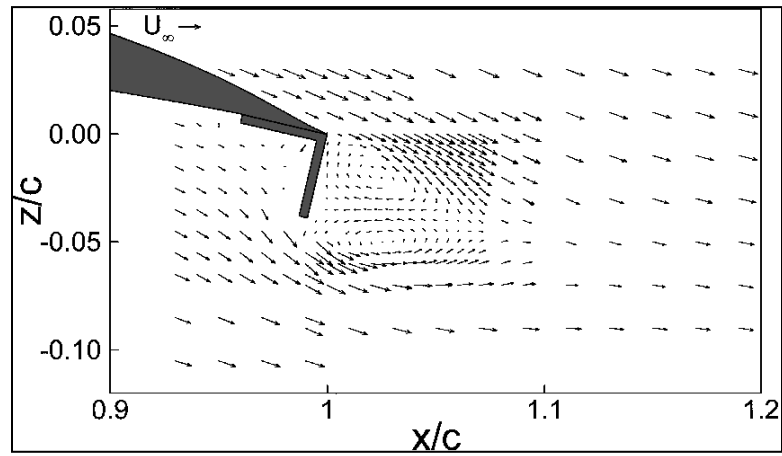


Figure 4: Mean velocity vectors aft of gurney flap[22]

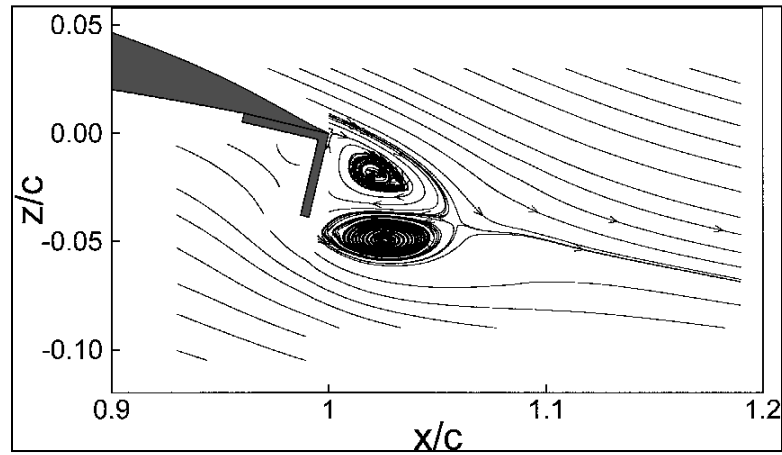


Figure 5: Time averaged streamlines for 4% Gurney flap at 0° AOA[22]

There is an increase in the pressure observed at the trailing edge which is explained to be caused by the stagnation of flow caused by the flap as it acts as a bluff body for the flow. The flow behind the flap is seen to be like the vortex shedding behind a bluff body like a cylinder. The counter rotating vortices shed at regular intervals are seen as shown in Figure 6.



**Figure 6: Vortex Shedding behind the Gurney Flap[22]**

Different mounting angles of the Gurney flap have been shown to produce different amounts of augmentation to the lift coefficient when compared to an airfoil with no gurney flap [23]. The lift increases with increase in the angle of flap deflection. Drag is also found to increase with increase in flap deflection angle. The maximum L/D is recorded for a gurney flap deflection of  $45^\circ$ . The zero lift angle of attack is also found to reduce with deflection of the gurney flap.

A jet flap creates a fluid sheet at the trailing edge which can be deflected using a small flap similar to a gurney flap. An alternate approach for its implementation is based on circulation control using a Coanda type trailing edge [24]. The results show that this technique can augment the lift significantly without a drag penalty during the cruise

conditions for jet momentum coefficients that are practically realizable in an unmanned aerial vehicle. The method used in the current work is based on deflecting a jet sheet via the small flap, which is deflected like a conventional control surface.

## UNCERTAINTY INFORMATION

The word “uncertainty” means doubt, and thus in its broadest sense “uncertainty of measurement” means doubt about the validity of the result of a measurement [25].

In statistical calculations, the standard deviation can be a measure of the most probable error or uncertainty, defined as

$$\sigma = \sqrt{\frac{1}{N} \sum_{i=1}^n (x_i - \bar{x})^2}$$

Here,  $N$  is the number of samples;  $x_i$  is the individual sample estimate,  $\bar{x}$  is the average of all estimates and  $\sigma$  is the standard deviation. Uncertainty information can also be gathered from the specification of a device used for measurement. In this thesis, uncertainties in various quantities have been reported where necessary.

## **CHAPTER II**

### **PROJECT SUMMARY**

The current work is the concluding effort of Phase II of the project, *UAV Hinge-less Flight Controls via Active Flow Control*. The objectives of Phase I were to demonstrate and test active flow control technology for lateral control and suppress stall, and study the feasibility of application on a UAV platform. Phase II of the project aims at designing, implementing the technologies and testing them onboard a UAV. The challenges faced in implementing the lab-tested technologies onboard are related to sizing of the systems, on-board power management for additional systems, managing space and weight, etc.

#### **PREVIOUS WORK AT TEXAS A&M UNIVERSITY**

At Texas A&M University, active flow control has been researched extensively and technologies such as synthetic jet actuators, gurney flaps and continuous and pulsed blowing have been explored as possible candidates for in-flight implementation for improving performance and as a replacement for conventional control surfaces. Serrated and slotted gurney flaps [26] have been tested and compared with a solid gurney flap to explore three-dimensional effects on aerodynamic performance. The results show a reduction in both lift and drag as compared to the solid gurney flap which resulted in overall increase in L/D. Also more explorations are reported in [27]. Jet flaps

have also been explored as a possible technology for UAV platforms for flight testing[28].

Preliminary work in implementing continuous blowing for roll control in flight, carried out at Texas A&M University[29] presents findings from a flight test of a modular blowing jet flap built inside the wing spanning about 7% of the wingspan of a 33% Extra 330S aircraft. The results show that the jet flap is capable of generating moments that could roll the aircraft. Studies investigating pulsed blowing for stall control[30] show dependence of gain in lift and delay in stall angle on the jet momentum and the frequency of pulsing.

## **CURRENT WORK**

The current work is a continuation of the effort to implement the lab-tested active flow control technology consisting of continuous blowing Trailing Edge (TE) actuator as alternatives to ailerons, and pulsed blowing Leading Edge (LE) actuator for stall suppression.

Chapter III presents the characteristics of the test vehicle. Chapter IV presents a review of the construction of LE actuator and TE actuator originally reported earlier[31]. The results from wind tunnel tests of the 33% Extra 330S aircraft from [31] have been deducted and analyzed for comparison of performance of the TE actuators with conventional ailerons and effect of LE actuator on stall suppression. Also, their combined use shows the synergy between them.

The following definitions are used:

*Coefficient of Jet Momentum,  $C_\mu$*

It is the ratio of the momentum of the air jet ejected out of the actuator to the momentum of the free-stream. For continuous blowing, average velocity across the span,  $V_{jet}$  is used to calculate the jet momentum. For pulsed blowing, jet velocity over averaged a period of time and across the span is used.

$$C_\mu = \frac{2h_{slot} V_{jet}^2}{cV_\infty^2} \quad \text{Eq (1)}$$

The coefficients of jet momentum for LE actuator and TE actuator are represented as  $LEC_\mu$  and  $TEC_\mu$  respectively.

*Reduced Frequency,  $F^+$*

Reduced frequency of the pulsed jet is the frequency of the jet,  $f$ , non-dimensionalized by a frequency parameter in terms of chord,  $c$  and free-stream velocity,  $V_\infty$ .

$$F^+ = \frac{fc}{V_\infty} \quad \text{Eq (2)}$$

In current research, the above two parameters have been used to characterize the fluidic actuators. They also serve as similarity parameters for fluidic actuators.

Pitch control actuator based on TE fluidic actuator (active elevator) is discussed in Chapter V. The energized air needed to drive the active elevator is provided to the elevator differently as compared to the TE actuators on the wings. Wind tunnel tests in a 3'×4' wind tunnel have been performed to compare the active aileron and the

conventional aileron. Also discussed is the design of the routing system for supplying the energized air to the active elevator in flight.

Chapter VI presents results from the flight tests comparison roll control authority of TE actuators and the conventional ailerons. The aircraft in various configurations has been put to flight tests in accordance with FAA regulations and requirements. No test flights are performed for pitch control and to demonstrate the use of LE actuator.

Chapter VII presents the conclusions and future work.

## CHAPTER III

### TEST VEHICLE

A Hanger 9® 33% scale Extra 330S ARF aircraft (Part No. HAN1175), as shown in Figure 7, has been selected to integrate and demonstrate the active flow control technology. The aircraft has been selected because of the following reasons:

1. It has a conventional wing-fuselage configuration similar to many existing unmanned aerial vehicles like the US military Global Hawk and Predator.
2. It has a thick NACA 0015 wing profile that provides space inside the wing for incorporating the fluidic actuators.
3. Its aerobatic nature provide the aircraft enough control to trim and turn effectively when the ailerons are reduced to the inboard 40% of their original length.
4. The developed technology is optimal for its incorporation into a low sweep, moderate to high aspect ratio wing form.
5. The excess power from engine helps lift the aircraft when heavier, active wings are installed.

The fuselage of the aircraft is made up of plywood and balsawood with built-up balsawood constructed wings, elevator and rudder. The vehicle is powered by a Zenoah® 80 cm<sup>3</sup> (GT-80) two-stroke twin cylinder spark ignition engine which supplies 6 bhp with a 24" × 10" wooden propeller (MA 2410B) at 7500 rpm. The vehicle's center

of gravity with batteries and without fuel has been established at the quarter chord location of the wings.

The specifications of the original configuration of the aircraft are given in Table 1.



**Figure 7: 33% scale Hanger9 Extra 330S ARF**

**Table 1: Specifications of 33% Extra 330S ARF**

Parameter	Value/ Type
Wing Profile	NACA 0015
Vehicle Span (B)	2464 mm
Vehicle Weight (W)	25 lb (11.36 kg)
Wing Surface Area (S)	12.15 ft <sup>2</sup>
Wing Loading (WL)	2.06 lb/ ft <sup>2</sup>
Engine Type	Air Cooled; 2 Stroke cycle type gasoline engine (GT-80)
Propeller	24" × 10" (MA 2410B), Wooden

## **CHAPTER IV**

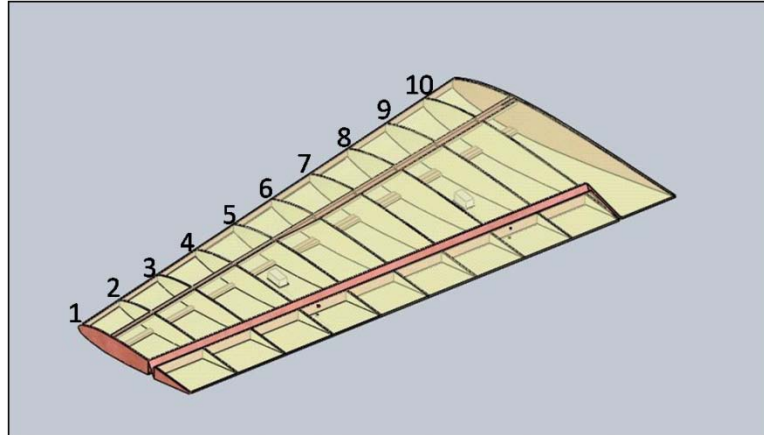
### **ROLL CONTROL AND STALL SUPPRESSION**

This section discusses the hardware modifications in the original wings of the aircraft, the construction and implementation of the LE and TE actuators and the results from wind tunnel studies carried out in the Oran Nicks 7'×10' wind tunnel at Texas A&M University.

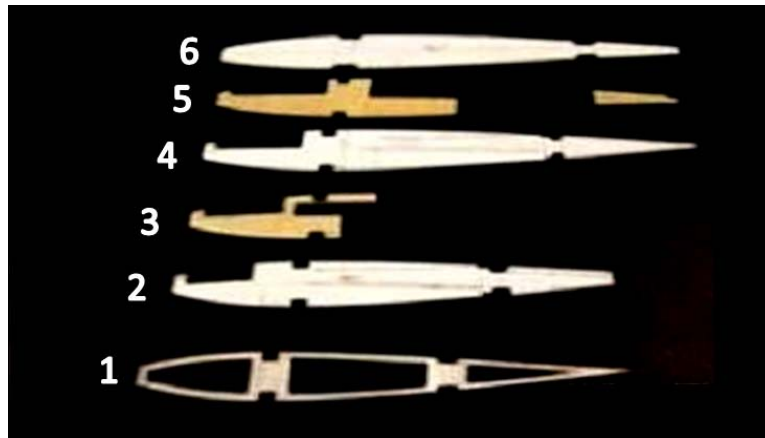
#### **HARDWARE DESIGN, CONSTRUCTION AND INSTALLATION**

Figure 8 shows the CAD model of the original wing. To accommodate the fluidic actuators, modifications have been made to the original wings. The ribs have been numbered starting from the wing tip. Ribs 1 through 7, originally made from balsa wood are removed without damaging the spars. Ribs 1 through 6 are replaced with 3 mm thick birch plywood ribs to improve load bearing capacity. Figure 9 shows the new ribs 1 through 6. Rib 1 is the wing tip rib and has been modified to serve as an inlet for the trailing edge fan modules as discussed later in this chapter and shown in Figure 19 on page 24. Ribs 2 through 5 have a cut on the leading edge side to accommodate the pulser module also discussed in detail later in this chapter. Ribs 4 and 5 are reduced to less than half of their length to accommodate motors used in the fan modules of TE actuator. Rib 7 has not been replaced to make space for the fan module for the pulser. No structural changes have been made to the ribs 8 through 10, the root section and the wing tube housing. The aileron has been reduced from the full span of 980 mm in the original

wing to an inboard aileron of length 400 mm, to accommodate the TE actuator's jet flap which takes the outboard location. The reduced aileron is supported by two hinge points to the main wing body and is controlled by a single servo located at its center.



**Figure 8: CAD model of the original wing**



**Figure 9: Modified Ribs 1-6 (Rib 1 is the wing tip rib)**

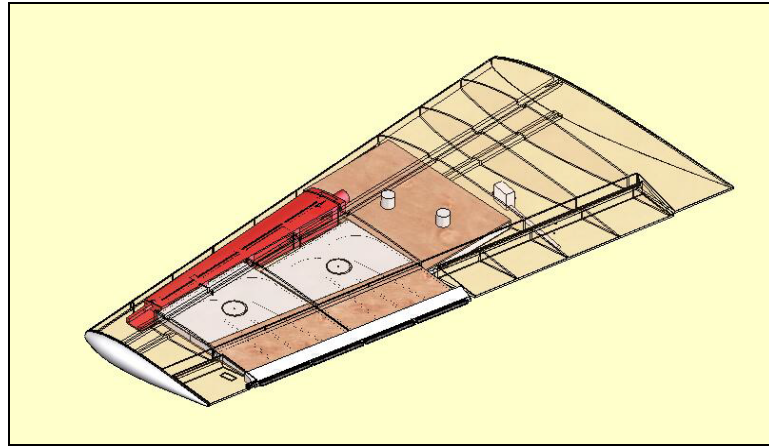


**Figure 10: CAD model of the active wing**

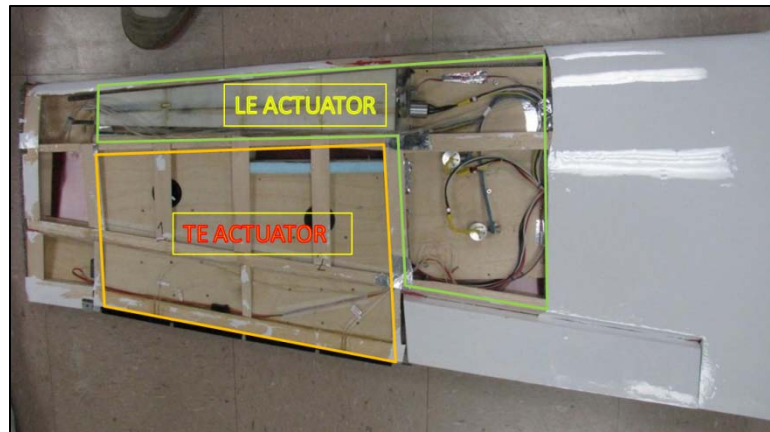


**Figure 11: Picture of the actual active wing with highlighted LE and TE actuators**

Each wing has a set of a LE actuator and a TE actuator. LE actuator is a pulsed-blowing system which produces and pulses air at desired  $F^+$  and desired  $C_\mu$  values, along the chord on the top surface of the wing. TE actuator is a continuous blowing and directing system which produces and controls a sheet of air jet along part of the trailing edge. The LE actuator and TE actuator can be seen in a CAD model of the active wing in

Figure 10 and a picture of the actual active wing with LE and TE actuators highlighted is presented in Figure 11.

The LE actuator and TE actuator are designed as modular systems. They are embedded in the wing where they are needed to be used as opposed to placing them in the fuselage. This eliminates the need for routing and saves weight. Also, this makes the systems easier to maintain as faults can be located in a module and corrected locally.

### **Leading Edge (LE) Actuator**

The LE actuator is designed to blow air pulses over the wing surface which will suppress flow separation over the wing at high AOA and hence delay stall. As a result, the aircraft's flight envelope is expected to increase due to increase in  $C_{L_{max}}$  which will enable short take off and landing and operation at high AOA.

The LE actuator is an assembly of the fan module and the pulser module. Figure 12 shows the LE actuator assembly. The block on the right is the fan module and the long extending member attached to it is the pulser module. The fan module (Figure 13) is fitted with two identical centrifugal fans from a household dust-buster driven by 12 V DC Astro Flight® 801V brushless motors working in tandem. Optical tachometers (OPB608A) measure the rpm of each of the fans. The housing of each fan in the module is based on a volute design which helps the air coming out radially outwards from the spinning fans' centrifugal exits to be directed towards the module exit where the two housings merge. The fan module extracts air from an opening underneath the wing surface close to the leading edge as shown in Figure 14. To make the inlet, the skin is removed and aluminum mesh is placed for strength and safety. The space between the

wing's pressure side skin and the bottom wall of the fan module acts as an intake plenum for the fans.

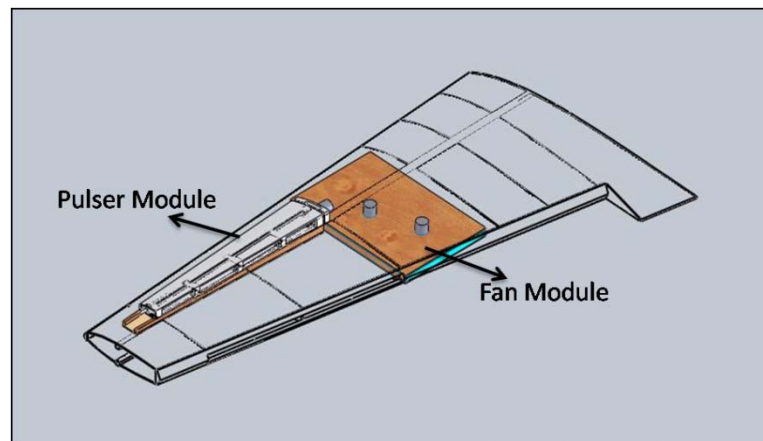


**Figure 12: CAD model of LE actuator embedded in the active wing**

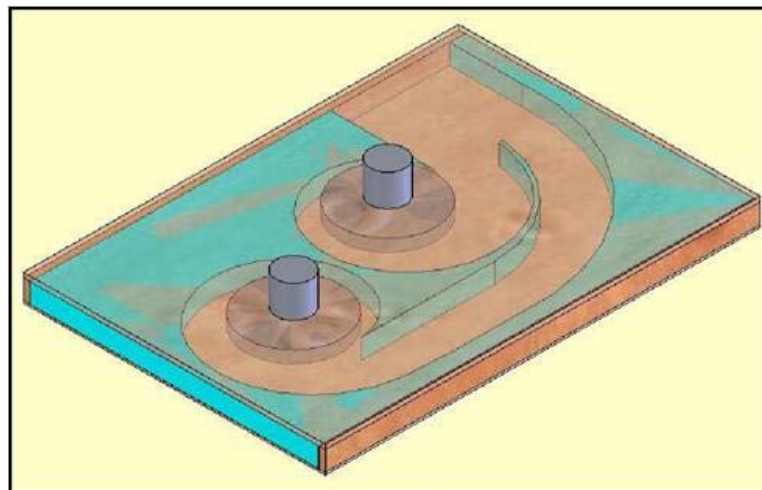


**Figure 13: Leading edge fan module**

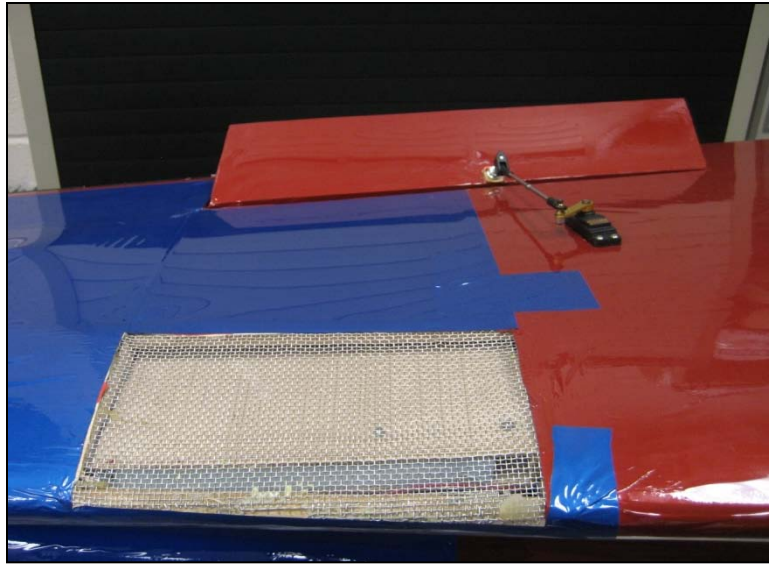


**Figure 14: Air inlet for LE fan module covered with aluminum mesh (underside view of the wing)**

The pulser module (Figure 15) consists of a delivery manifold and a pulser sub-assembly that sits on top of the delivery manifold. The delivery manifold, which directly interfaces with the fan module acts as a high pressure chamber as it is continuously fed with air by the fan module. Constructed from basswood, it spans 440 mm along the wing span and is placed 100 mm from the wing-tip. To promote span-wise uniformity of the flow out of the pulser slot, the delivery manifold tapers towards the tip so that the cross sectional area on the tip side is about one third of that on the root side.

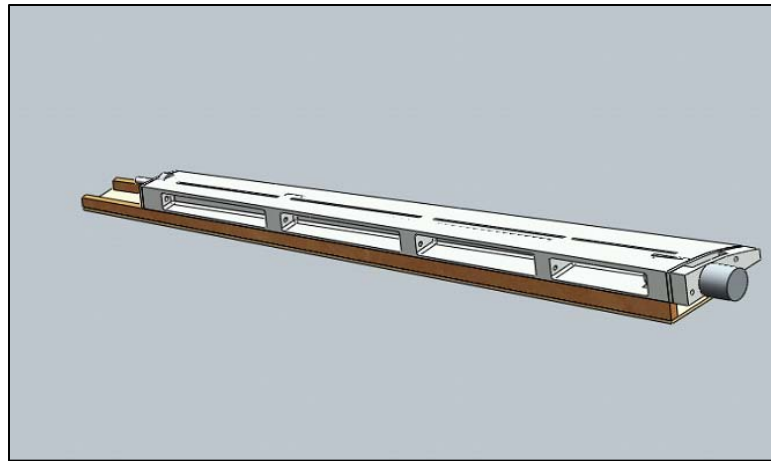


**Figure 15: Pulser module**

The pulser sub-assembly consists of a pulser housing (Figure 15), pulser shaft, bushings, gearbox and a 12 V Astro Flight® 801V brushless motor. Figure 16 shows the pulser rod, bushings and parts of housing. The pulser shaft, machined from an aluminum rod is 440 mm long and has a diameter of 4.8 mm. It has a 25 mm long pin on each end which is supported in the bearings on both ends. The shaft has a 3.2 mm wide through slot with three support ribs which prevent the shaft walls from bulging at high rotational speeds. To reduce the eccentricity in rotation, the shaft is supported by a ball bearing at each end and three oil-impregnated bronze sleeve bushings. The pulser shaft is driven by a 12V DC Astro Flight 801V brushless motor via a 2:1 reduction gearbox (Figure 17). The gear reduction provides torque to overcome the starting friction of the pulser shaft as it rotates in bearings and bushings. The rpm of the pulser shaft is recorded by an optical tachometer (OPB608A) sensor installed in the gearbox wall and the reflector installed on the driven gear. The top surface of the pulser housing has a NACA 0015

profile to merge with the top surface of the wing. Air is ejected tangentially on the wing surface through four 1.5 mm wide slots along the span.

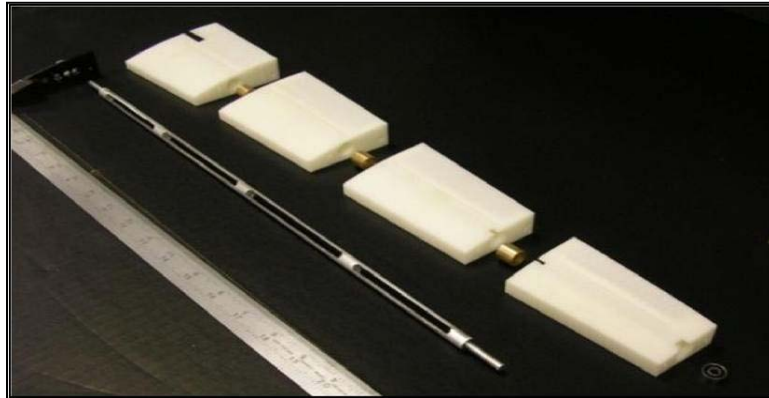


**Figure 16: Parts of pulser sub-assembly**

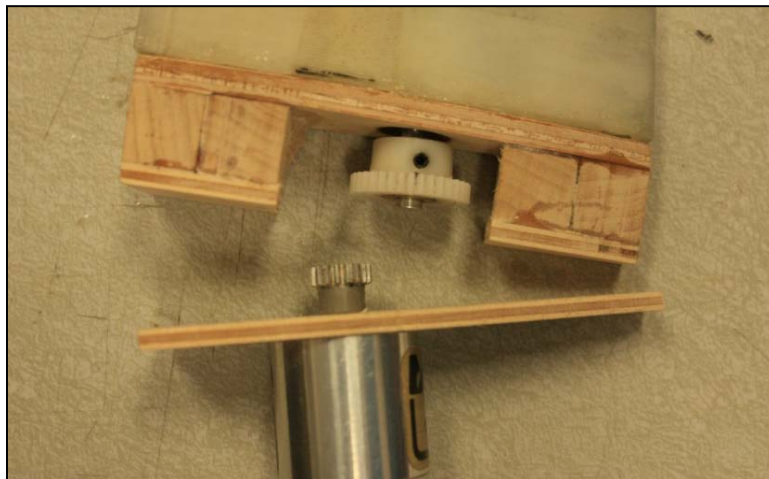


**Figure 17: Reduction gear for driving the pulser**

The placement of the LE actuator is based on the results from the wind tunnel tests[30] performed on a NACA 0015 airfoil at Texas A&M University. These tests

were partly aimed at finding the effect of pulsed blowing at 10% chord location and 50% chord location. The results show that for the 10% chord location case, there is an angle of attack range over which the pulsed air blowing is successful in delaying stall. Also, when pulsed blowing was performed at 50% chord location, the flow reattachment was not visible but the maximum lift coefficient was higher than the 10% case.

The actual placement of the jet slot exit was at 15% chord location because of the leading edge wing spar, which, along with the design of the pulser module, effectively constrained the position of the jet exit slot to 15% of chord location.

### **Trailing Edge (TE) Actuator**

The trailing edge (TE) actuators (shown in Figure 18) produce a sheet of air that can be deflected up or down to alter the wing's circulation and the differential circulation on both wings results in aircraft roll. The elimination of the conventional aileron removes the contour breaks on the wing surface and is expected to improve the stealth characteristics of the aircraft. The TE actuator spans 440 mm and extends up to 100 mm from the wing tip. The actuator is a combination of two similar blocks placed side by side. The two-block design reduces the structural changes and provides strength as it allows a rib running between the two blocks. This also enables better serviceability as faults do not require a full system overhaul.

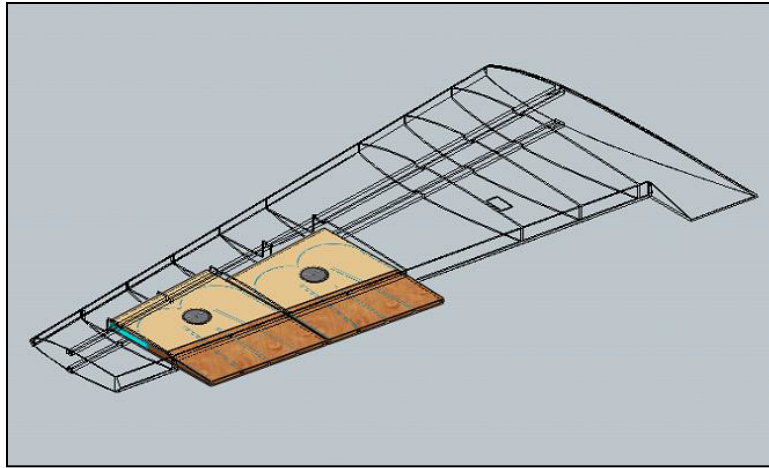


**Figure 18: CAD model of the TE actuator embedded in active wing**

Each block of the TE actuator consists of a fan module which actuates part of the trailing edge with a nearly uniform sheet of air jet that can be deflected up to  $\pm 45^\circ$  with respect to the chord line. The base plate of the fan module is made out of 3 mm thick birch plywood and acts as a mounting plate for the fan motor. The air for the fan inlets for both blocks is drawn from the wing tip as the wing tip rib is made hollow and covered with aluminum mesh. To facilitate induction of the air, the wing tip rib (rib number 1 shown in Figure 19 ) is covered by aluminum wire mesh cloth. The space between the top plate of the fan module and wing skin acts as the inlet plenum for the fans and the air can enter the fans from the top of the blocks. The top plate is made up of 1.5 mm thick Birchwood plywood. Figure 20 shows a fan module block under its cover plate. The housing design of the TE actuator's fan module is different from that of the LE actuator. In this case, the housing design enables the air to be directed from the fan

into a sheet that is spread along the trailing edge. The housing walls taper from 12.5 mm to 5 mm into the converging plenum and act as flow straighteners.



**Figure 19: A view of wing tip rib (rib 1)**



**Figure 20: TE actuator block fan module**

Straightened air enters into a converging plenum which ends into a mouthpiece (Figure 21). The mouthpiece for the trailing edge jet is made out of peach wood and has a 4.8 mm wide through slot for the exit of the air jet. The jet flap which is responsible for directing the jet up or down is machined from a 2.5 mm wide steel plate and has been supported by aluminum bushings. The opening between the walls of the mouthpiece and the jet flap is 2.75 mm at its maximum deflected position of  $\pm 45^\circ$ . Figure 22 shows a detailed view of the jet flap.

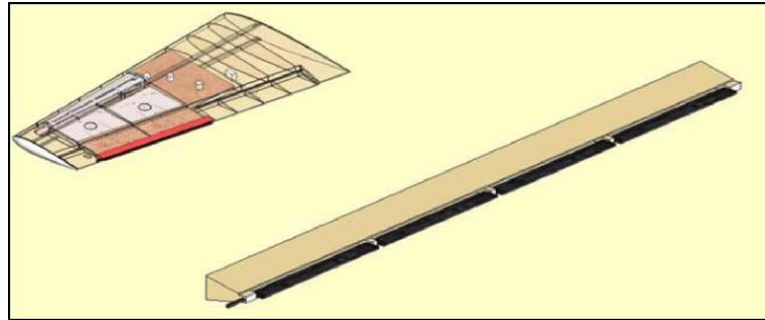


**Figure 21: CAD Model of the mouthpiece, full active wing in inset**

The deflection of the jet flap is controlled by a JR® digital servo motor DS368BB, located on the far tip side of the wing. Figure 23 shows a view of the servo for controlling the jet flaps.



**Figure 22: Detailed view of jet flap deflected up**

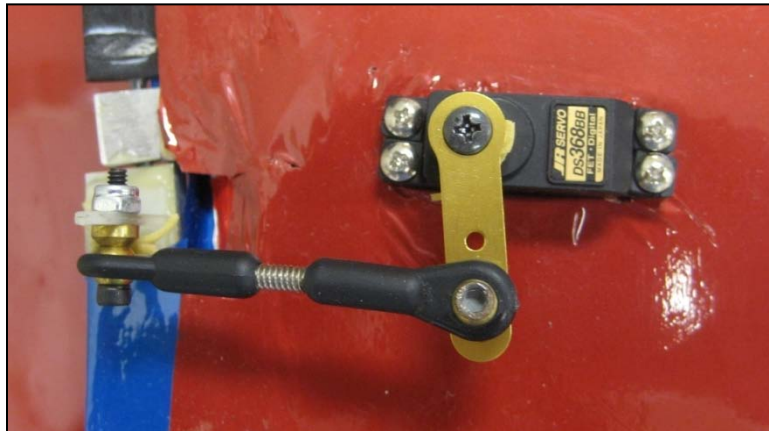


**Figure 23: Micro servo for controlling jet flap**

Besides the active wings, there is another set of wings that is constructed called heavy wings. Heavy wings are a replica of active wings in terms of mass distribution. These wings are constructed as dummy wings to test the lifting characteristics of the vehicle with heavier wings without risking the active flow control components on the

active wings. Figure 24 shows a picture of heavy wings under construction. The dummy blocks of wood can be clearly seen.

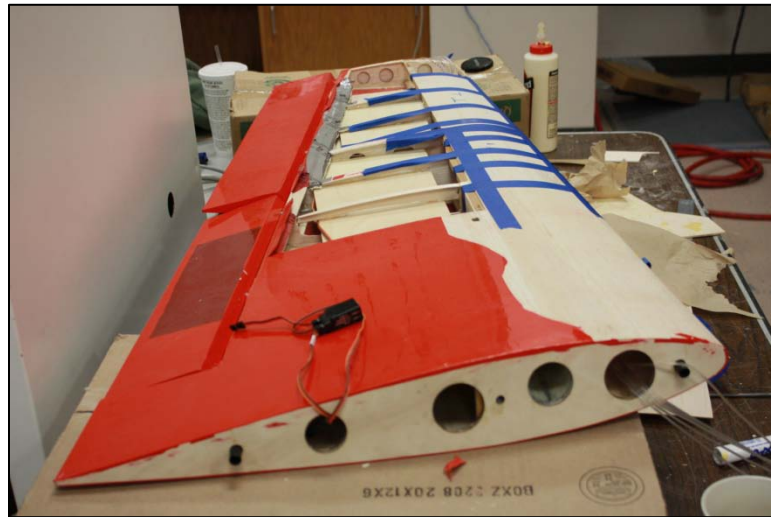


**Figure 24: Heavy Wings under construction**

The active wings and heavy wings are heavier than the original wings by about 6 lb (2.72 kg) each. Also, the avionics including the flight computer and other instrumentation installed in the fuselage account for an increase in vehicle weight. So, the installation of the wings increase the take-off weight to 45 lb (20 kg), thereby pushing the wing loading to 3.70 lb/ft<sup>2</sup>.

Table 2 shows the weight and wing loading of the aircraft with new wings and accompanying avionics.

**Table 2: Comparison of vehicle weight and wing loadings**

Configuration	Weight (W)	Wing loading (WL)
Original Wings	25 lb	2.06 lb/ft <sup>2</sup>
Original Wings with avionics	33lb	2.71 lb/ft <sup>2</sup>
Active/ Heavy Wings with avionics	45 lb	3.70 lb/ft <sup>2</sup>

## WIND TUNNEL TEST SETUP

**Figure 25: 33% Extra 330S aircraft mounted in 7'×10' wind tunnel**

The wind tunnel tests were conducted in the 7'×10' Oran W. Nicks low speed wind tunnel facility at Texas A&M University. The details can be found in [31]. For the acquisition of force and moment data, the model was mounted using a three-strut support on an external balance located immediately below the test section as shown in Figure 25. The wind tunnel flow characteristics are shown in Table 3.

**Table 3: Characteristics of Oran W. Nicks low speed wind tunnel[31]**

Parameter	Value/ Type
Maximum Tunnel Velocity	300 ft/s (~91.5 m/s)
Dynamic Pressure Variation	$\pm 0.4\%$
Dynamic Pressure Resolution	$\pm 0.5 \text{ lb/ ft}^2$
Flow Angularity	$\pm 0.25^\circ$
Static Pressure Gradient	0
Turbulence Factor	1.1
Turbulence Intensity	$< 1\%$
Entry Boundary Layer Thickness	1.5 in
Exit Boundary Layer Thickness	3.5 in

## CONFIGURATIONS AND TEST MATRICES

The wind tunnel tests on LE and TE actuators as reported in [31] are carried out following values of rpm of motors and the parameters,  $LEC_\mu$ ,  $TEC_\mu$  and  $F^+$ .

- LE actuator fan motors running at 11,000 rpm yield  $LEC_\mu = 0.0275$  at  $V_\infty = 17 \text{ m/s}$ .
- LE actuator pulser motor running at 2500 rpm produces  $F^+ = 1$ .
- TE actuator fan motors running at 11,000 rpm yield  $TEC_\mu = 0.0075$  at  $V_\infty = 17 \text{ m/s}$ .
- TE actuator fan motors running at 11,000 rpm yield  $TEC_\mu = 0.0024$  at  $V_\infty = 30 \text{ m/s}$ .

The wind tunnel tests and flight tests are carried out at the above mentioned parameters at three configurations: Basic, Reduced and Active. More details are presented in Table 4.

**Table 4: Configurations of full scale wind tunnel test**

	<b>Basic</b>	<b>Reduced</b>	<b>Active</b>
Wings	Heavy	Active	Active
Ailerons	Full Span	Reduced	Reduced
Aileron Deflection (°)	0, 15, -15	0, 15, -15, 30, -30	0
Elevator Deflection (°)	0, 15, -15	0, 15, -15	0
Jet flap Deflection (°)	NA	0	0, 45, -45; $TEC_\mu = 0.0075, 0.0024$
LE actuator/ Pulser	NA	NA	$LEC_\mu=0.0275, F^+ = 1$

Other key points of interest are:

- The tests involving TE actuators are carried out at one setting of rpm of the fans.  
The two free-stream velocity values, 17 m/s and 30 m/s provide two values of  $TEC_\mu$ . The tests involving LE actuators are carried out at only 17 m/s. This allows only one value of  $LEC_\mu$  and  $F^+$  each.
- The pitching moment is measured about the quarter chord line of the wings.  
Also, the center of gravity of the vehicle was set at quarter chord location by adding ballast weight.
- LE actuator tests were only conducted for  $F^+=1$  which has been chosen to be the optimum frequency for maximum effectiveness of pulsed blowing in separation control[30].

- Deflection convention: Positive deflection means upward deflection. For Example  $-15^\circ$  deflection is downward deflection for both ailerons and elevator. Also, L $15^\circ$ R- $15^\circ$  represents left aileron deflection of  $15^\circ$  upwards and right aileron deflection of  $15^\circ$  downward.
- Reduced Ailerons correspond to the inboard ailerons which have been retained as backup ailerons and to compare the effectiveness with TE actuators in wind tunnel tests.

**Table 5: Test matrix for Basic configuration**

Run No.	Aileron ( $^\circ$ )	Elevator ( $^\circ$ )	$V_\infty$ (m/s)
6	0	0	30
7	0	15	30
8	0	-15	30
9	L15R-15	0	30
10	L15,R-15	15	30
11	L15,R-15	-15	30
12	0	0	17
13	0	15	17
14	0	-15	17
15	L15,R-15	0	17
16	L15,R-15	15	17
17	L15,R-15	-15	17

### Configuration 1: Basic

Table 5 provides the summary of tests conducted in the wind tunnel on the basic configuration of the aircraft.

### Configuration 2: Reduced

Table 6 provides the summary of tests conducted in the wind tunnel on the reduced configuration of the aircraft.

**Table 6: Test matrix for Reduced configuration**

Run No.	Aileron (°)	Elevator (°)	$V_{\infty}$ (m/s)
18	0	0	30
19	L15, R-15	0	30
20	0	0	17
21	L15, R-15	0	17
22	L30, R-30	0	30
23	L30, R-30	0	17

### Configuration 3: Active

Table 7 provides the summary of tests conducted in the wind tunnel on the active configuration of the aircraft.

**Table 7: Test Matrix for Active configuration**

Run No.	Jet Flap Deflection(°)	$TEC_{\mu}$	Pulser $F^+$	$LEC_{\mu}$	$V_{\infty}$ (m/s)	Comments
24	L0,R0	0.0024	0	0	30	TE active, no deflection
25	L45,R-45	0.0024	0	0	30	
26	L-45,R-45	0.0024	0	0	30	both TE jet flaps deflected down
28	L45,R-45	0.0075	0	0	17	
29	L-45,R-45	0.0075	0	0	17	both TE jet flaps deflected down
30	L45,R-45	0	0	0	30	gurney flap equivalent
31	L45,R-45	0	0	0	17	gurney flap equivalent
39	L0,R0	0.0075	1	0.0275	17	
40	L45,R-45	0.0075	1	0.0275	17	
41	L-45,R-45	0.0075	1	0.0275	17	both TE jet flaps deflected down
42	L-45,R45	0.0075	1	0.0275	17	
43	L-45,R45	0.0024	0	0	30	

## PLOT SUMMARY

Table 8 summarizes the plots that have been compiled from the above tests.

**Table 8: Plot summary for wind tunnel tests**

<b>Result Number</b>	<b>Result Description</b>	<b>Run numbers plotted</b>
1	Characteristics of Basic configuration at 17 m/s	12,13,14,15
2	Comparison of all configurations with no deflections at 30 m/s	6,18,24
3	Comparison of $C_{RM}$ for all configurations at $TEC_\mu=0.0024$ and 0.0075	6,9,19,22,30,25 and 12,15,21,23,31,28
4	Comparison of $C_{RM}$ for Active configuration at $TEC_\mu=0.0024$ and 0.0075	24,25,43,28
5	Effect of pulser on $C_L$ at $F^+=1$ , $LEC_\mu=0.0275$ , at $TEC_\mu=0.0075$	12,20,39
6	Effect of pulser at $LEC_\mu=0.0275$ on $C_{RM}$ at $TEC_\mu=0.0075$	39,28,40,42
7	Effect of pulser at $LEC_\mu=0.0275$ , $F^+$ , both jet flaps deflected down, at $TEC_\mu=0.0075$ on $C_L$	26,29,39,41

## RESULTS

### Characteristics of Basic Configuration at 17 m/s

Figure 26 shows the variation of  $C_L$ ,  $C_D$ ,  $C_{PM}$  and  $C_{RM}$  for the aircraft in the basic configuration. The first three plots show the variations of  $C_L$ ,  $C_D$  and  $C_{PM}$  for three positions of elevator i.e.  $-15^\circ$ ,  $0^\circ$  and  $+15^\circ$ . It is evident from the plots that the  $C_L$  Vs AOA for three elevator deflections vary a little in slope and are shifted by nearly equal amounts for equal variation in deflection. The  $C_D$  for elevator  $15^\circ$  and  $0^\circ$  varies a little for the range of AOA but the  $-15^\circ$  exhibits more drag especially at AOA greater than  $5^\circ$ . As expected, the  $C_{PM}$  Vs AOA are offset by equal amounts for equal difference in deflections.

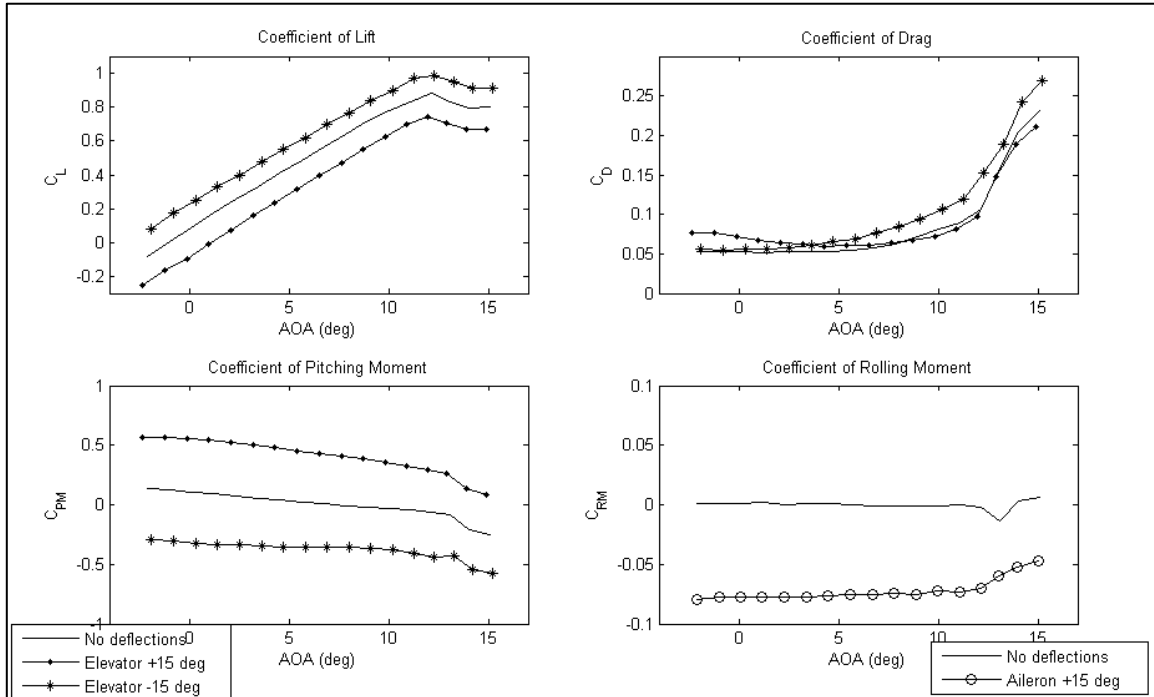
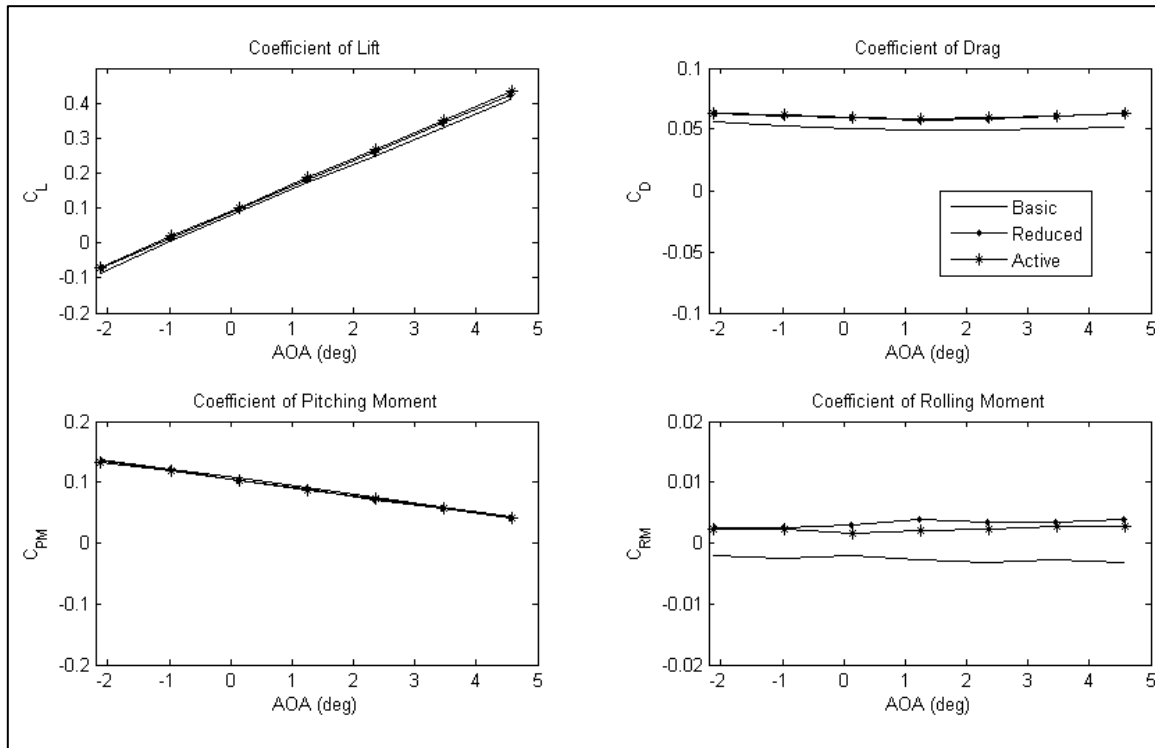


Figure 26: Characteristics of aircraft in conventional configuration at 17 m/s

The fourth plot (right bottom corner) shows the  $C_{RM}$  for  $0^\circ$  and  $15^\circ$  deflection of ailerons (L $15^\circ$ , R- $15^\circ$ ).

### Comparison of All Configurations with No Deflections at 30 m/s

Figure 27 shows the coefficient of rolling moment comparison for no deflections of all three configurations at 30 m/s. Note that the for the active configuration, the jets on the TE actuators are running but the jet flap is not deflected. The LE actuator is also not running.



**Figure 27: Comparison of characteristics of Basic, Reduced and Active Configurations with no deflections at 30 m/s**

Following are the inferences from the above plots:

- $C_L$  Vs. AOA plots for three wings are nearly similar.
- The reduced wing and active wing show very similar drag for the range of AOA, higher than the drag values of the conventional wing.
- $C_{PM}$  is practically the same for all three wings over the range of AOA
- $C_{RM}$  for the reduced wing is positive as compared to negative value for conventional wing. Also the active wing shows further positive value of  $C_{RM}$ . These differences may arise purely from manufacturing imperfections and are taken care of in flight by trimming the ailerons or TE actuators.

#### **Comparison of $C_{RM}$ for all configurations at $TEC_\mu=0.0024$ and $0.0075$**

Figure 28 shows comparison of  $C_{RM}$  at 30 m/s for the all configurations and

Figure 29 shows the comparison at 17 m/s.

Following are the inferences from the above plots:

- Basic Configuration full span wings at L15°, R-15° aileron deflections are the most effective in producing rolling moment as expected for both airspeeds.
- Reduced Configuration, L30°, R-30° aileron deflections are second most effective for both airspeeds.
- Reduced Configuration with L15°, R-15° follow in the order of effectiveness. They are almost half as effective as L30°, R-30° deflections for both speeds.
- TE actuators at  $TEC_\mu=0.0024$  are about half as effective as Reduced Ailerons at L15°, R-15°. At  $TEC_\mu=0.0075$ , they are almost as effective as Reduced Ailerons

at  $L15^\circ$ ,  $R-15^\circ$ . This indicates that rise in  $TEC_\mu$  has resulted in better control authority.

- The Gurney flaps are more effective at 17 m/s as compared to 30 m/s.

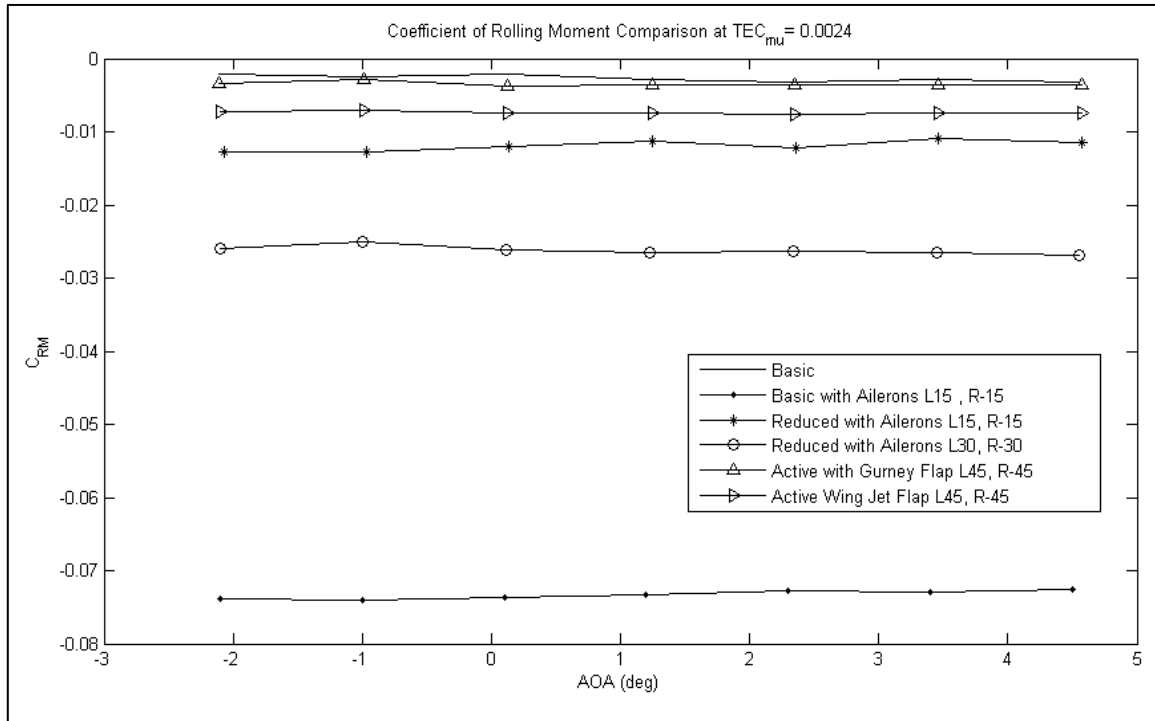
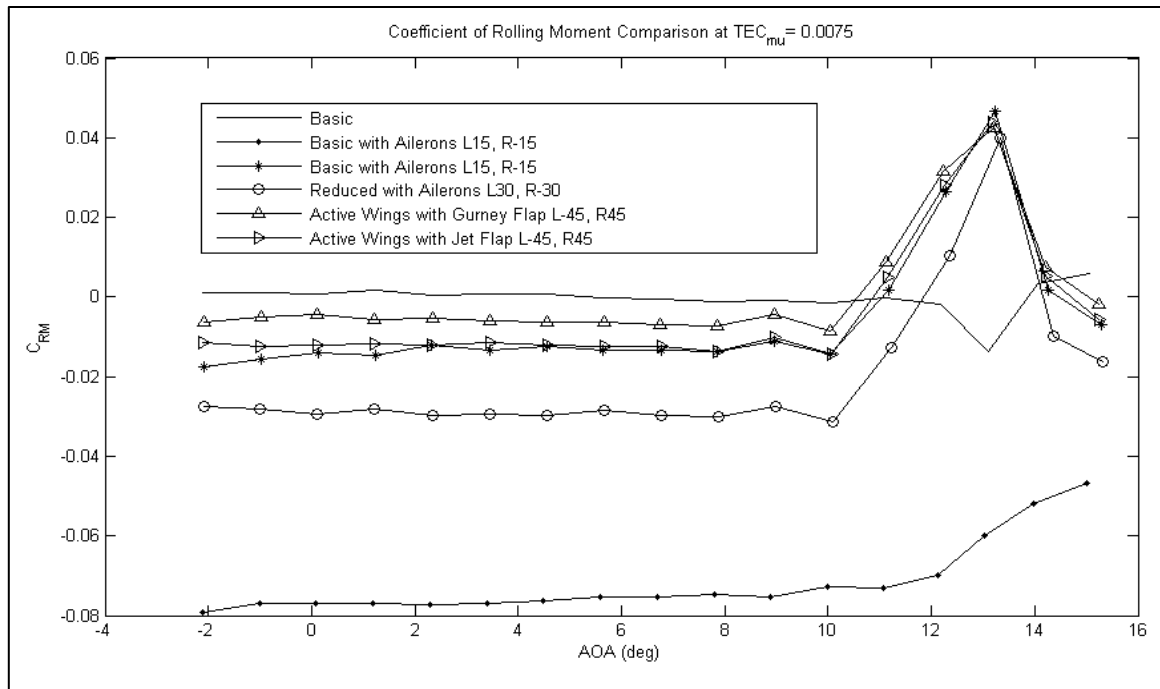


Figure 28: Comparison of  $C_{RM}$  at  $TEC_\mu$  of 0.0024



**Figure 29: Comparison of  $C_{RM}$  at  $TEC_{\mu}$  of 0.0075**

It is noteworthy here that, the  $C_{RM}$  for TE actuators is about half of that obtained by reduced ailerons at  $15^\circ$  deflections, yet it provides enough control to successfully trim and bank the aircraft as will be evident from flight test results in Chapter VI. The chosen aircraft is acrobatic and has much more control with full ailerons than needed to control the aircraft in basic turns and to trim the aircraft.

### Comparison of $C_{RM}$ for Active Configuration at $TEC_\mu=0.0024$ and $0.0075$

Figure 30 shows the comparison of  $C_{RM}$  for active wing with TE actuators at following configurations:

1. Active Configuration, jet active,  $L0^\circ$ ,  $R0^\circ$
2. Active Configuration,  $TEC_\mu = 0.0024$ , Aileron deflections:  $L45^\circ$ ,  $R -45^\circ$
3. Active Configuration,  $TEC_\mu = 0.0024$ , Aileron deflections:  $L-45^\circ$ ,  $R 45^\circ$  (reverse)
4. Active Configuration,  $TEC_\mu = 0.0075$ , Aileron deflections:  $L45^\circ$ ,  $R -45^\circ$

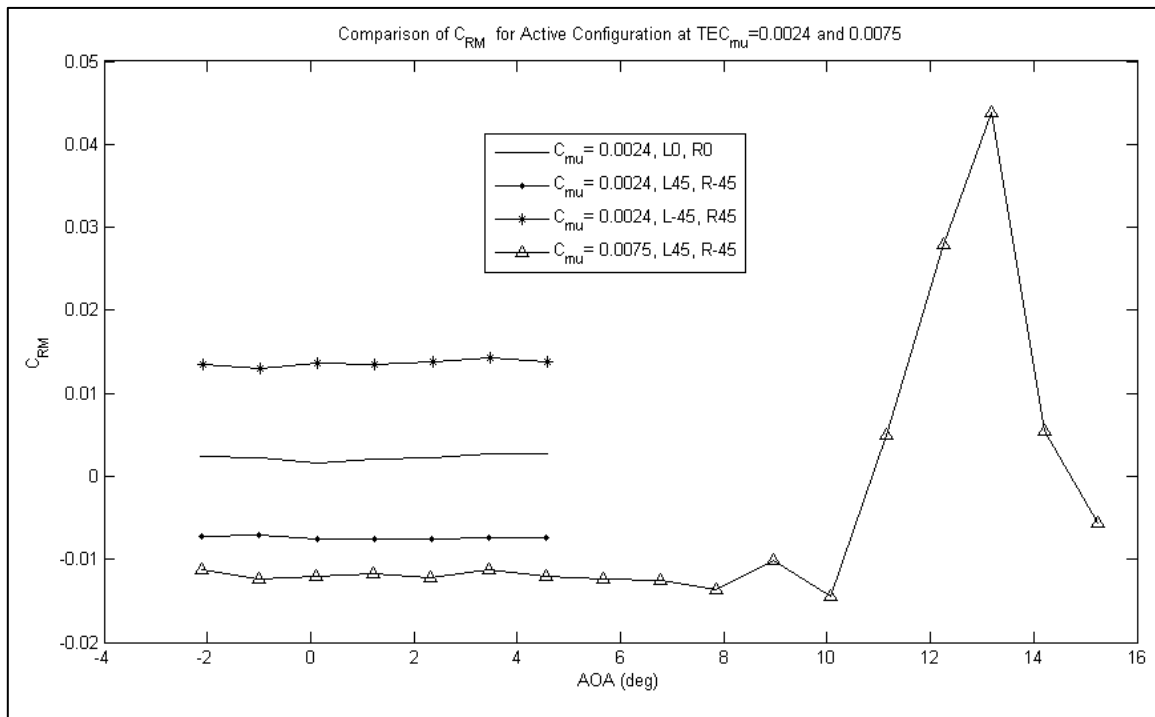
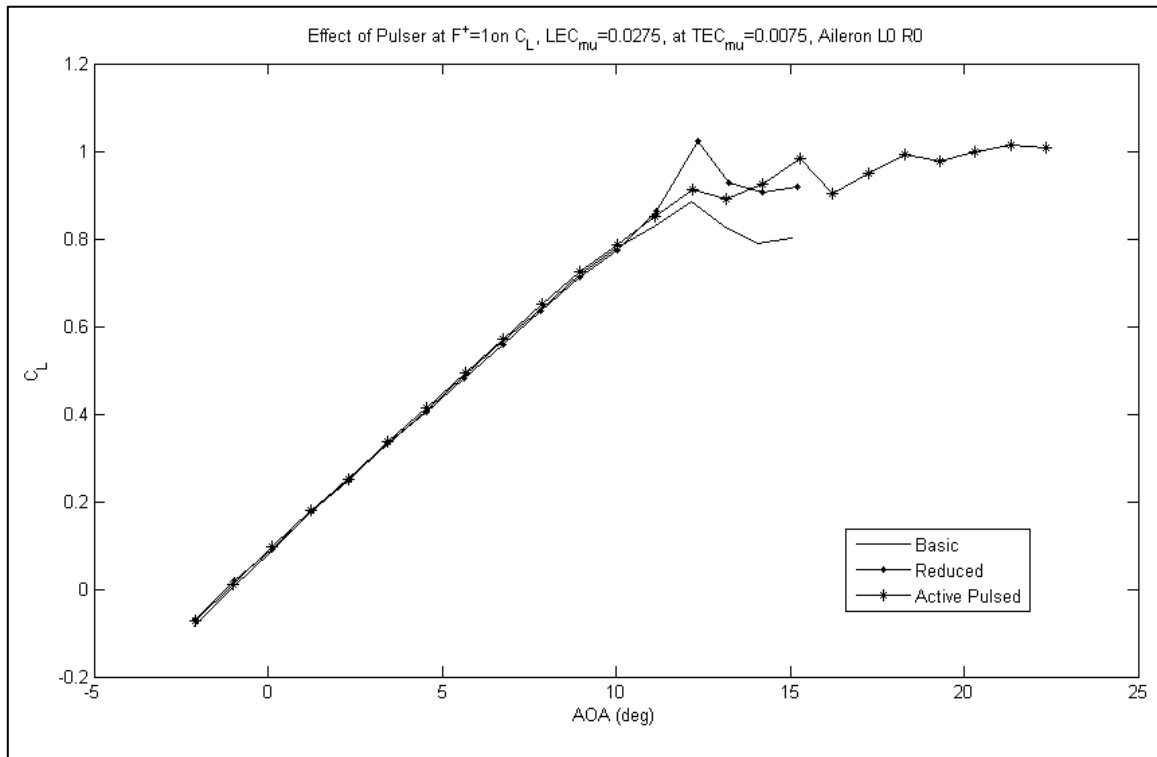


Figure 30: Comparison of  $C_{RM}$  for Active configuration at  $TEC_\mu=0.0024$  and  $0.0075$

This plot compares the effect of  $TEC_\mu$  and deflection reversal on control effectiveness. It is evident that deflection reversal reverses the effectiveness by equal magnitude as expected. Also, the effectiveness at  $TEC_\mu = 0.0075$  is about 50 percent higher than the effectiveness at  $TEC_\mu = 0.0024$ .

**Effect of Pulser on  $C_L$  at  $F^+=1$ ,  $LEC_\mu=0.0275$ , at  $TEC_\mu=0.0075$**

Figure 31 shows the effect of LE actuation at  $F^+=1$  on  $C_L$  Vs AOA.



**Figure 31: Effect of pulsed blowing at  $F^+=1$  on  $C_L$  and  $LEC_\mu = 0.0275$  at  $TEC_\mu = 0.0075$**

The wings with reduced ailerons have higher  $C_{L_{max}}$  as compared to conventional wings.

The LE pulsed blower has favorable effects on  $C_L$ . Stall was delayed practically until at least  $22^\circ$  which was the upper limit of AOA that could be reached during the test.

### Effect of Pulser at $LEC_\mu=0.0275$ on $C_{RM}$ at $TEC_\mu=0.0075$

Figure 32 shows the effect of LE Pulser on  $C_{RM}$ .

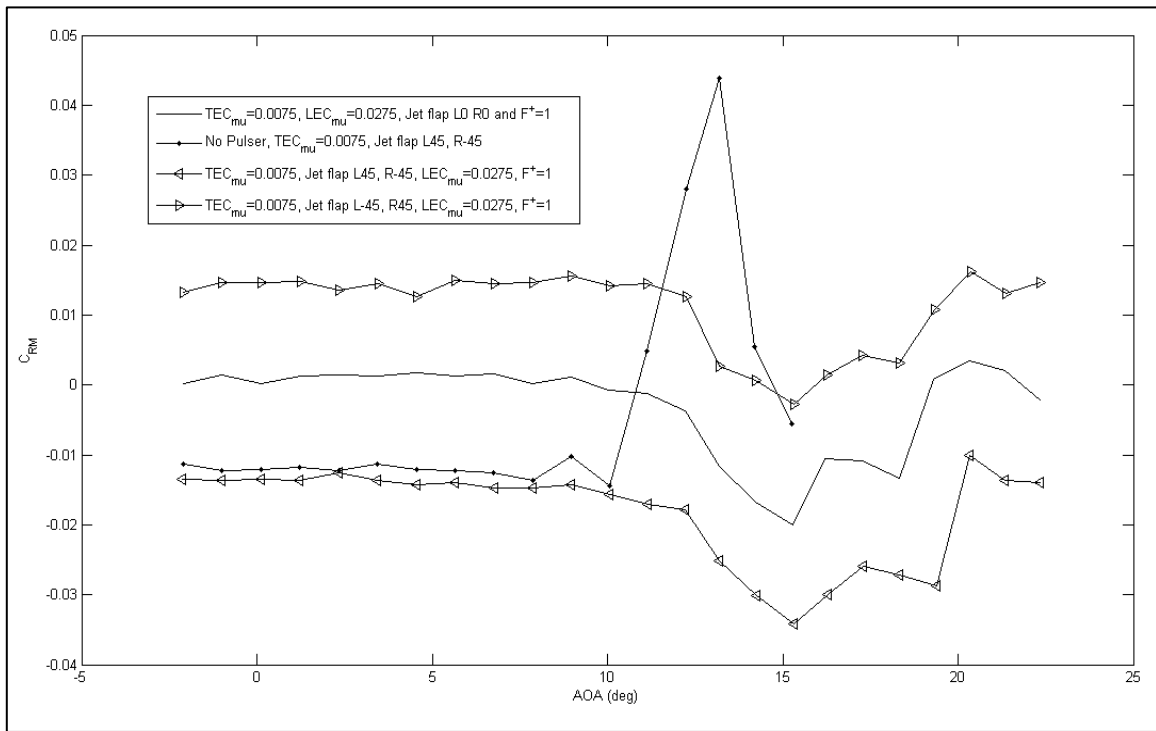
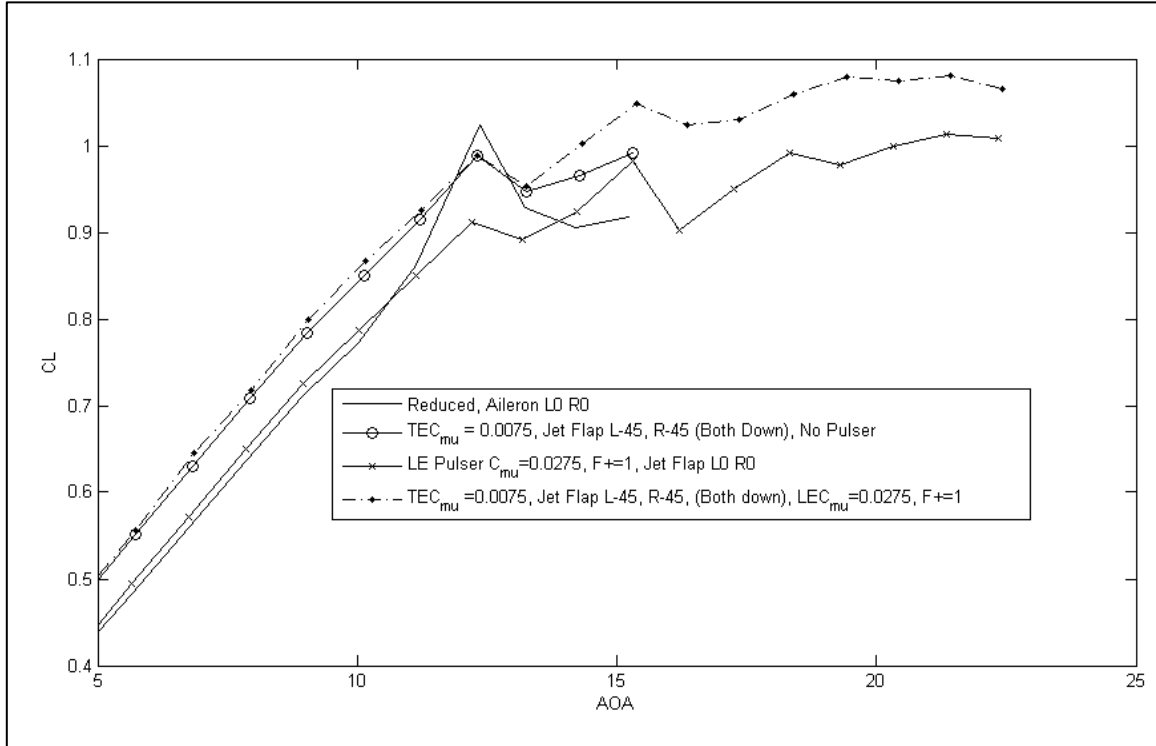


Figure 32: Effect of LE Pulser at  $LEC_\mu=0.0275$ ,  $F^+=1$  on  $C_{RM}$  at  $TEC_\mu=0.0075$

It is interesting to note that the LE pulser increases the  $C_{RM}$  marginally. This suggests some synergy in LE pulser and TE jets. In other words, LE actuation with pulsed blowing is helping the TE actuators to produce more roll.

**Effect of LE Pulser on  $C_L$  at  $LEC_\mu=0.0275$ ,  $F^+=1$ , Both Jet Flaps Deflected Down,  
at  $TEC_\mu=0.0075$**



**Figure 33: Effect of LE Pulser at  $LEC_\mu=0.0275$ ,  $F^+=1$ , both jet flaps deflected down, at  $TEC_\mu=0.0075$   
on  $C_L$  Vs. AOA**

Figure 33 shows the synergy observed when LE actuator and TE actuator are operated together with TE jet flaps deflected down on both wings. Without LE actuator and jet flap deflection, the stall angle is around  $12^\circ$ . TE jet flaps when deflected down on both wings, sustain the  $C_{L_{max}}$  up to  $15^\circ$  and reduce the intensity of stall. When LE actuator is used without the TE jet flaps, the stall angle gets delayed up to the

measurable limit of  $22^\circ$ . Interestingly, LE pulser and TE jet flaps sustain  $C_{L_{max}}$  to 22 degrees and at a much higher value of  $C_{L_{max}}$  when compared to the LE pulser only case. This suggests a clear synergy between LE pulser and TE jet flaps in increasing  $C_{L_{max}}$  and sustaining it at much higher values delaying stall. The increase is nearly 10% over the pulser-only case.

Table 9 presents the uncertainty information for quantities pertaining to the measurement in 7'×10' wind tunnel.

**Table 9: Uncertainty in measured quantities in 7'×10' wind tunnel tests**

<b>Quantity</b>	<b>Uncertainty</b>
Uncertainty in force measurement	0.1% of maximum value
Uncertainty in moment measurement	0.1% of maximum value
Uncertainty in dynamic pressure measurement	0.4% of maximum value
Uncertainty in measuring $LEC_\mu$ and $TEC_\mu$	5% of maximum value

## SUMMARY OF FULL SCALE WIND TUNNEL TEST

The wind tunnel tests demonstrate substantial control by TE actuators: half as much as reduced ailerons ( $15^\circ$  deflection) at  $TEC_\mu=0.0024$  and nearly equal to that with reduced ailerons ( $15^\circ$  deflection) at  $TEC_\mu=0.0075$ . The LE pulser has successfully been able to delay stall and maintain  $C_{L_{max}}$  with some fluctuations up until at least  $22^\circ$  as compared to a normal stall angle of about  $12^\circ$ . The rolling capability increases when TE actuators are operated in combination with LE actuator. TE actuators deflected in the same direction (down) resulted in sustaining  $C_{L_{max}}$  to about  $15^\circ$  as compared to normal  $12^\circ$  stall angle. When LE pulser was operated in combination with TE jet flaps deflected down, there was nearly  $10^\circ$  increase in  $C_{L_{max}}$  recorded as compared to the pulser only case.

## **CHAPTER V**

### **PITCH CONTROL**

Pitch control using active flow control is achieved by replacing the port side of the horizontal tail, hereby referred as the conventional elevator, with a modified control surface, hereby referred to as the active elevator. The air to be supplied to the active elevator is generated inside the fuselage by two fan modules and transferred to the elevator by a duct called the elevator duct. Wind tunnel studies have been performed to compare the characteristics of the conventional and the active elevator. Design of routing air to the active elevator in flight has been described. No flight testing is performed involving pitch control.

#### **DESIGN AND CONSTRUCTION OF ACTIVE ELEVATOR**

In order to implement active flow control in pitch control, an existing conventional elevator has been modified and fitted with TE fluidic actuator. Figure 34 and Figure 35 show the conventional elevator and the active elevator respectively. Table 10 presents the comparison in the specifications of the elevators.



**Figure 34: Conventional elevator**



**Figure 35: Active elevator**

**Table 10: Specifications of conventional and active elevators**

Specification	Conventional Elevator	Active elevator
Mean Chord Length, c	275mm	275 mm
Span	480 mm	480 mm
Surface Area	0.128 m <sup>2</sup>	0.128 m <sup>2</sup>
Volume	0.002565m <sup>3</sup>	0.002565m <sup>3</sup>
Aspect Ratio	1.8	1.8
LE sweep Angle	9.3°	9.3°
Jet slot width	-	3.5 mm
Jet Flap Deflection	-	± 45°
Jet Flap Length (%c)	-	7 mm (2.6% of c)

As can be seen in Figure 35, the joint between the stabilizer and the control surface as seen in conventional elevator in Figure 34 is missing. In fact, the two parts have been integrated so that the rear part acts as a plenum for the air entering through the root side. Figure 36 shows the detailed view of the active elevator with arrows dictating the flow path inside.

Energized air enters from a rectangular opening in the root section and leaves the trailing edge as shown in Figure 36. The direction of ejected air is controlled by a jet flap which is supported at multiple locations across the span. Also seen are the baffles which are responsible for turning of the flow. The jet flap is energized by a small servo motor JR MC-35. Figure 37 shows the jet flap deflected upward.

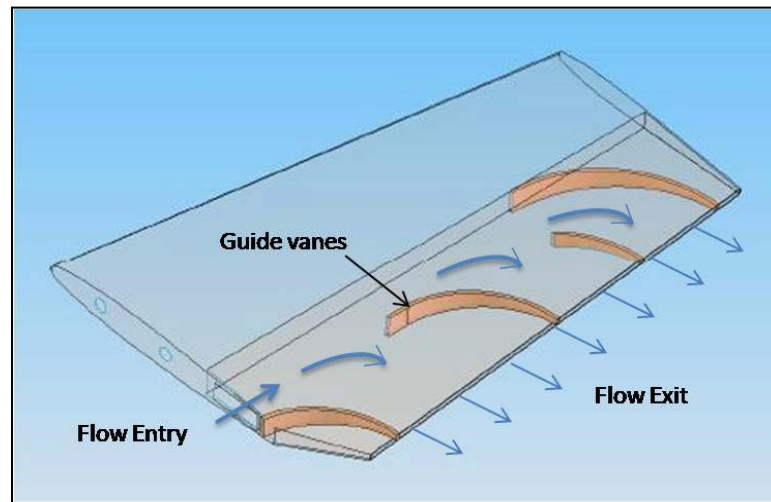


**Figure 36: Detailed view and flow path for active elevator**



**Figure 37: Jet Flap Deflected upward**

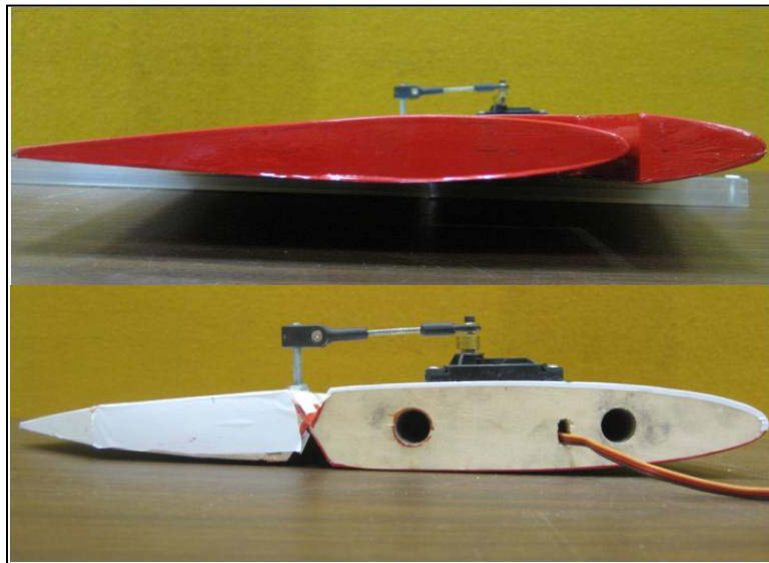


**Figure 38: Airfoil profile comparison for conventional airfoil (top) and active airfoil (bottom)**

Figure 38 shows the side view of the two elevators to present a comparison of the airfoil profiles. It can be seen that the active elevator has slightly more thickness as compared to the conventional elevator.

## **ELEVATOR DRIVING SYSTEM**

The active elevator requires a supply of air on-board. This air is supplied by two elevator fan modules and a duct that merges the air from the elevator fan modules to the elevator inlet.

### **Elevator Fan Modules**

Figure 39 shows a view of one of the two fan modules mounted in the fuselage with detail in inset. This fan module contains an Astro Flight 801V brushless motor and

a dust-buster fan in housing. The inlet of the module faces outward and sucks air from the side of the fuselage and exit of the module is a rectangular slot which interfaces with the elevator duct described below.

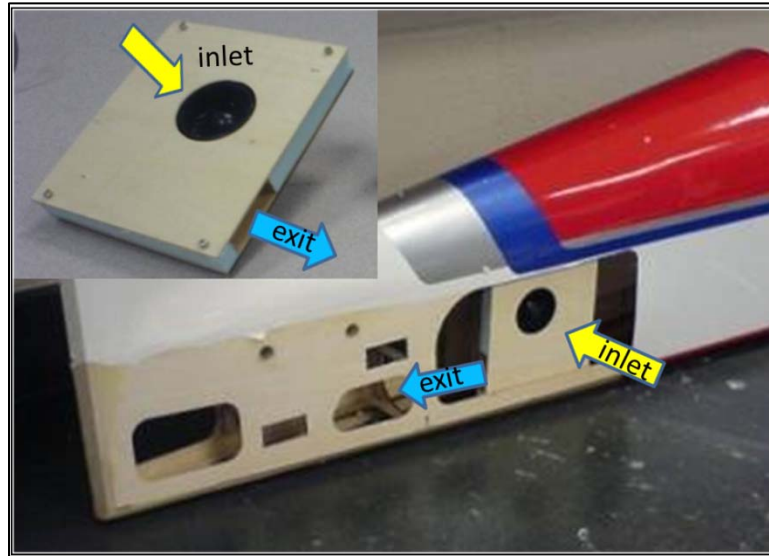
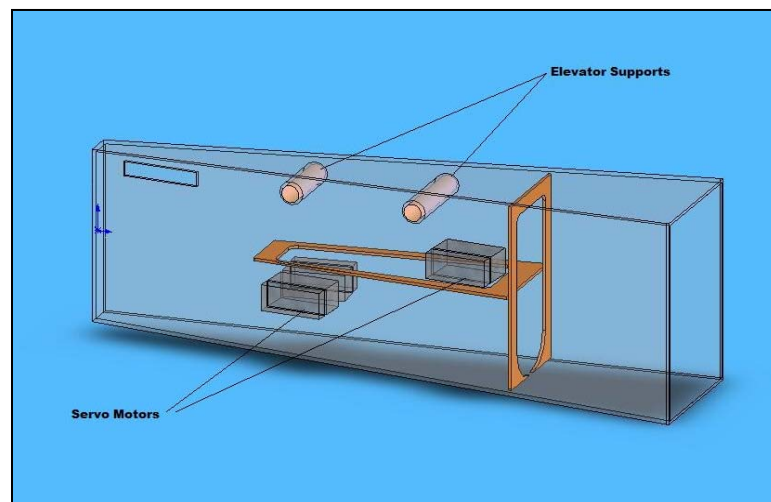


**Figure 39: One of the fan modules for pitch control**

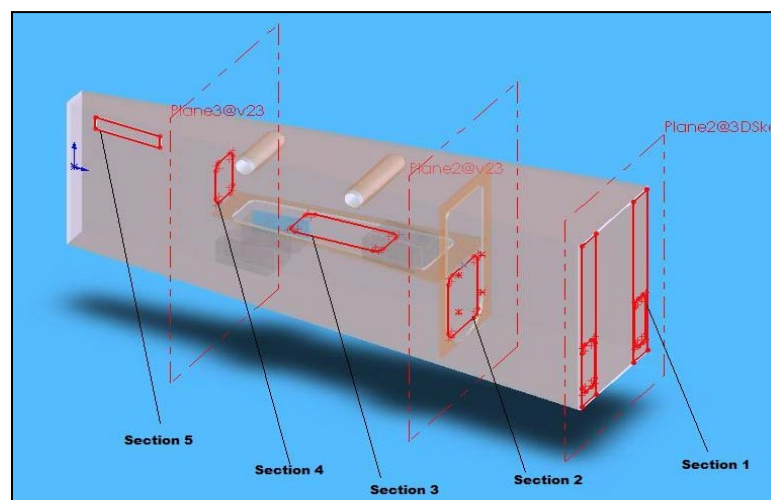
### **Elevator Duct Design**

Figure 40 shows the CAD model of the inside of the rear section of the fuselage of the aircraft. It has components like the servo motors and elevator supports which were not moved. Also there are sections for strength which cannot be removed or damaged. The rectangular opening in the root section of the active elevator mates with the rectangular opening near the end of the fuselage. Figure 41 shows the identified sections which provide an estimate of the space that is available for design of the elevator duct. Figure 42 shows the CAD model of the elevator duct as designed. The first section is in

two parts. Each of these parts mates with the exit of a fan module. Section 2 collects the air and supplies it further to section 3 which is designed with baffles (detail seen in inset) to promote straightening of flow as it turns through a small area and a sharp bend. Figure 43 shows parts of the actual elevator duct.



**Figure 40: CAD model of fuselage rear section of the aircraft**



**Figure 41: Identified sections for designing elevator duct**

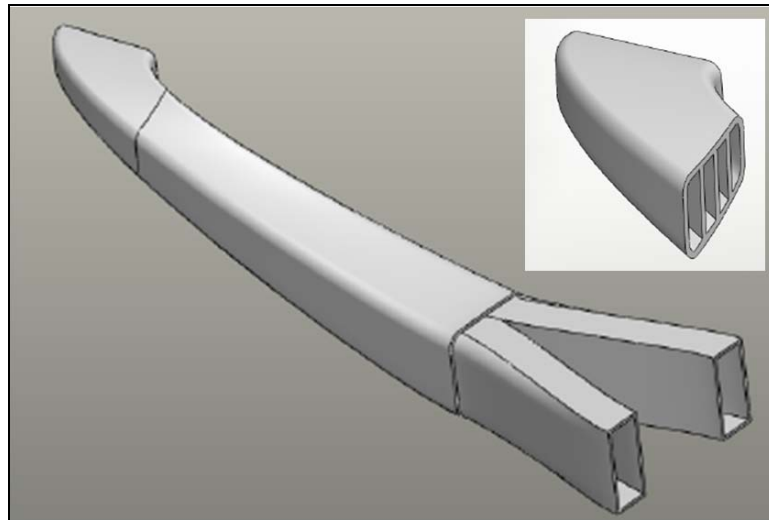


**Figure 42: CAD model of elevator duct (section 3 detail in inset)**



**Figure 43: Picture of the Actual elevator Duct Parts**

## ACTIVE ELEVATOR PERFORMANCE

The setup for mounting and powering the active elevator for measuring the performance (jet exit velocity and velocity profile along the span) of the active elevator is the same as that used in the wind tunnel and will be discussed in detail in next sub-section.

Velocity has been measured using a TSI® model 1201 disposable hot wire probe at a sampling rate of 1000 samples per second. A TSI® IFA-300 constant temperature anemometer has been used which can sample at the maximum rate of 250,000 samples per second. The jet flap is supported by three inner supports in the span, creating 4 sections of the span. Two location points are placed in each section dividing each section uniformly. These are the eight location points Figure 44 where hot wire measurements have been taken.

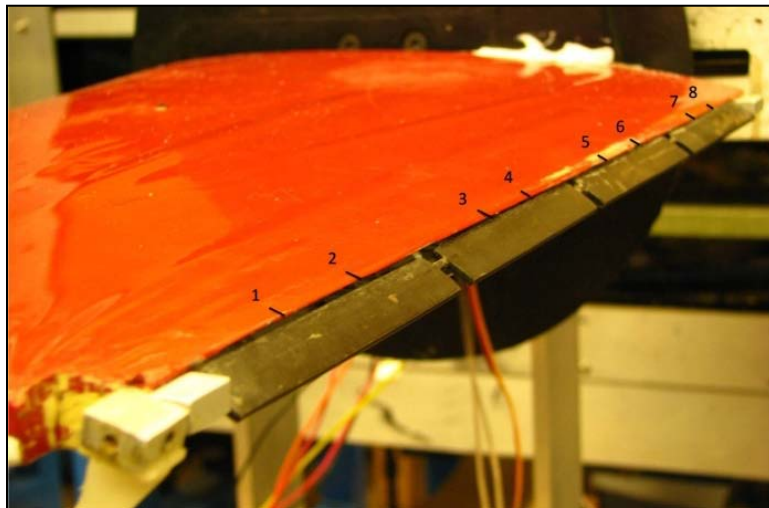


**Figure 44: Numbered locations for measuring velocity profile**

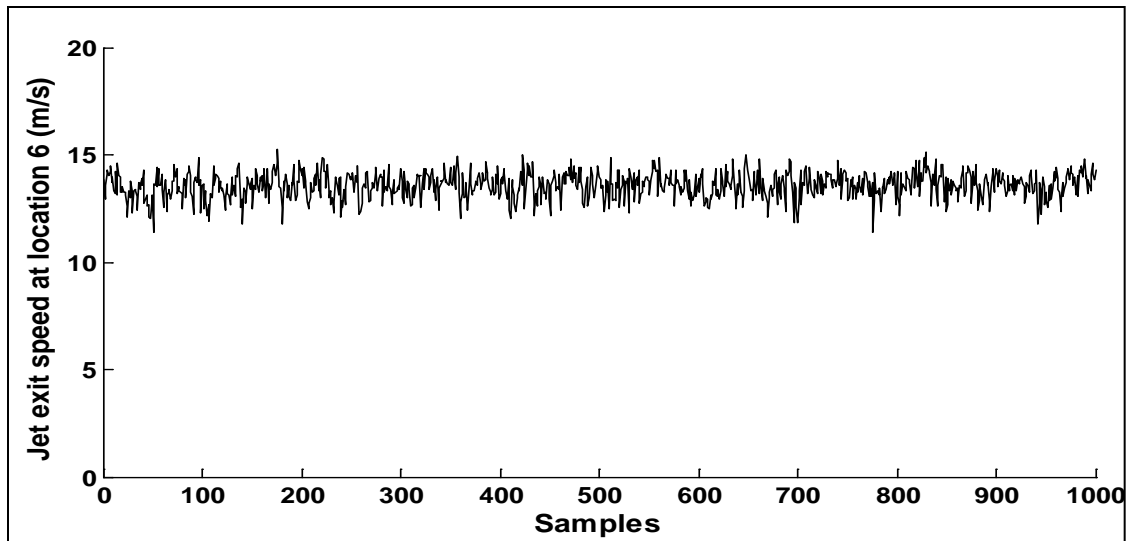


**Figure 45: Jet velocity at location 6**

Figure 45 shows velocity values for 1 second (1000 values) at location 6 for 10,000 rpm. The results show a mean exit velocity of 13.6 m/s and a standard deviation of 0.624 m/s. Figure 46 shows the velocity profile generated plotting the mean values of velocity at all 8 location points. Average velocity of the jet across the span = 10.3 m/s. The jet exit velocity is lower for locations 7 and 8 because of the severity of turn as these locations are at the root side of the elevator.

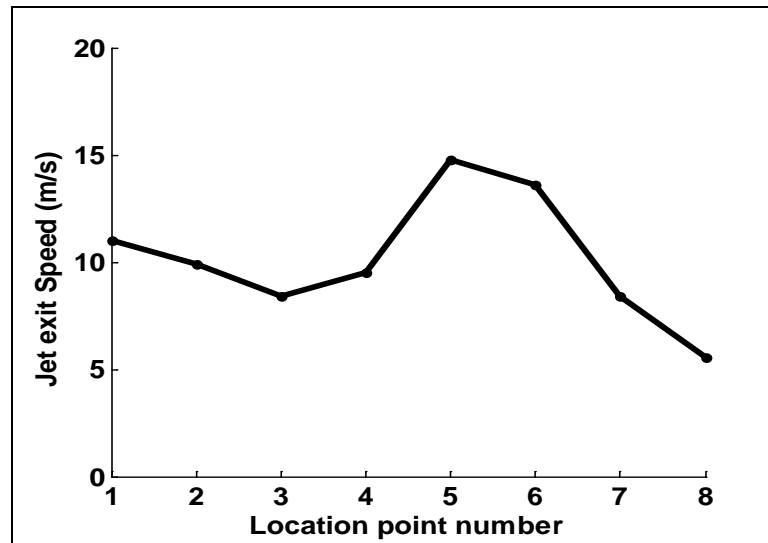


Figure 46: Velocity profile across 8 locations

Also, the guide vane between location 5 and location 4 directs more flow into location 5 and 6 which makes jet exit velocity at these locations higher. There is some scope in this area for future work to optimize the location and shape of guide vanes to ensure maximum uniformity. Using Equation 1,  $ELC_{\mu} = 0.0067$  at 20 m/s free-stream velocity at 10000 rpm of fan motors.

## WIND TUNNEL TEST

Comparison tests between conventional and active elevator were conducted at Texas A&M University's  $3' \times 4'$  wind tunnel facility at a free stream velocity of 20 m/s, yielding a Reynolds number of around  $3.75 \times 10^5$  based on elevator chord length. This section discusses the hardware and the mounting setup that was designed for mounting the elevator so that it can experience similar conditions and constraints as expected in flight.

The elevator fan module motors run at 10,000 and 14,000 rpm for this test. As previously mentioned,  $ELC_\mu$  at 10,000 rpm is 0.0067. The  $ELC_\mu$  value at 14,000 rpm is not measured but is expected to be higher than 0.067.

## Hardware

A 6-component force balance from API® Industrial Automation has been used for the force and moment measurement. The force balance can measure up to  $\pm 300$  N of force and 30 N-m of torque. The output voltages from the balance are measured using a 16-bit A/D board with a clock speed of 250 kHz per channel. The wind tunnel turbulence intensity of the tunnel is less than 0.3%, assuming isotropic turbulence. The free stream velocity was measured using a wall mounted pitot static probe with a tip diameter of 3.175 mm. The pressure and velocity measurement were carried out using Flowkinetics TM FKS 1 DP-PBM manometer. Wind tunnel corrections for solid and wake blockage and for streamline correction were applied using the methodology described in Rae and Pope[32]. An optical encoder is used to measure the real time angle of the model and its output is fed through a National Instruments® data acquisition card, NI USB-6211 into LabVIEW®. A Vexta two phase stepper motor (Model number PK264B2A-SG18) with a damper (Model number D6CL-6.3F), capable of generating a torque of 5 Nm, controlled by a micro LYNX® 4/7 micro stepping motor controller is used for changing the AOA of elevator. The stepper motor has 200 steps per revolution, wherein the micro LYNX® allows micro-stepping up to 51,200 steps per revolution. The model angle of attack can be adjusted within an accuracy level of  $0.05^\circ$ .

## **Elevator Mounting Setup**

The mounting setup of the elevator is required to allow for a continuous supply of air and also allowing for change in AOA during test. In addition it was also required to measure the real AOA during the test. These requirements drove the design of the elevator mount which is shown in Figure 47. The mechanism is mainly manufactured in-house from aluminum. The active elevator is mounted on two carbon shafts exactly how it is mounted on the aircraft. A duct rapid prototyped from ABS plastic transfers the air to the elevator inlet. The air is provided by a fan module similar to the one powering the LE actuator in the wings. To match the in-flight conditions and constraints, the fan modules operate same number and type of fans and motors and same supply of power as intended for the in-flight fan modules. The only difference in this setup and the in-flight setup is the type of duct used and the fact that the in-flight fan modules are in two parts instead of one. The elevator is mounted via a mounting plate on the force balance. The drive from the stepper motor is transferred to the elevator axis by a combination of gears. The combination: elevator, mounting plate and the fan module can rotate freely when the stepper motor is rotated. This way, the residual forces and moments of the combination can be tared out and only aerodynamic forces and moments may be recorded. Also an optical encoder measures the actual AOA of the setup which rotates about the quarter chord axis.

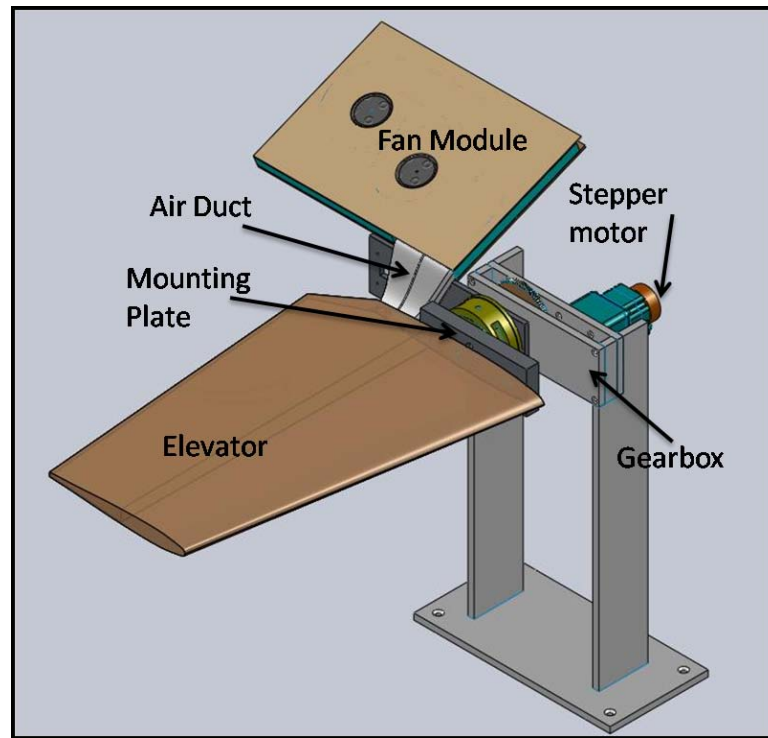


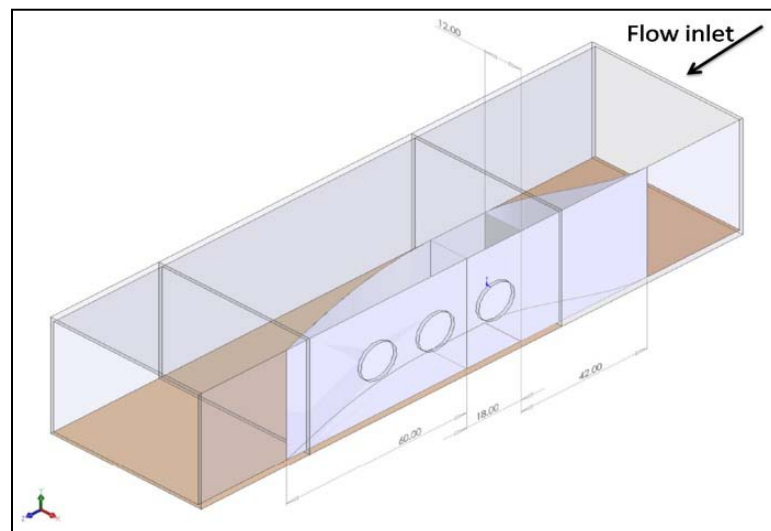
**Figure 47: 3D view of elevator mount apparatus**

The data acquisition has been carried out using LabVIEW® based virtual instrumentation. The program has the capability to pitch the model at a desired angle of attack while the tunnel is running, record all six components of the force and torque; tunnel speed, real time angle of attack and deflection of the control surface. The rpm of the jet driving fans can be controlled and monitored through the program. The data is written in Microsoft Excel® worksheets and is later reduced using MATLAB® for non-dimensionalization, application of boundary corrections and plotting.

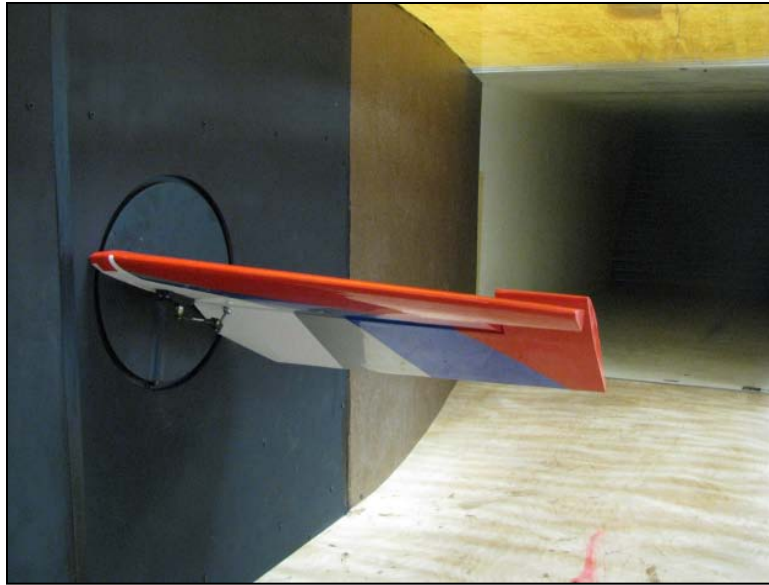
### **Test Section Preparation**

Figure 48 shows the CAD model of modified test section. The elevator mounting setup has been placed inside the original test section which is 4' wide. A new wall has

been constructed from plywood, and plexi-glass which leaves the actual test section with a converging-diverging wall. The diverging section slope is kept 1 in 5 to minimize the effects of any separation of flow. Also, the center section of the wall is made removable to provide access to the setup behind the wall. Figure 49 shows a picture of the conventional elevator mounted inside the modified test section. It can be seen that only the elevator is visible inside the test section. A circular plate that can also be seen in the plane of the wall is built around the mounting plate. This plate made from plexi-glass, maintains is about 5 mm distance from the wall and rotates with the elevator when the AOA is changed. Figure 50 shows the plate without the center section of the wall. This circular plate ensures that the AOA can be changed with a constant supply of air from fan module and forces and moments can be measured without errors due to contact and friction.



**Figure 48: Modified test section**



**Figure 49: Front side view of the elevator mounted in test section**

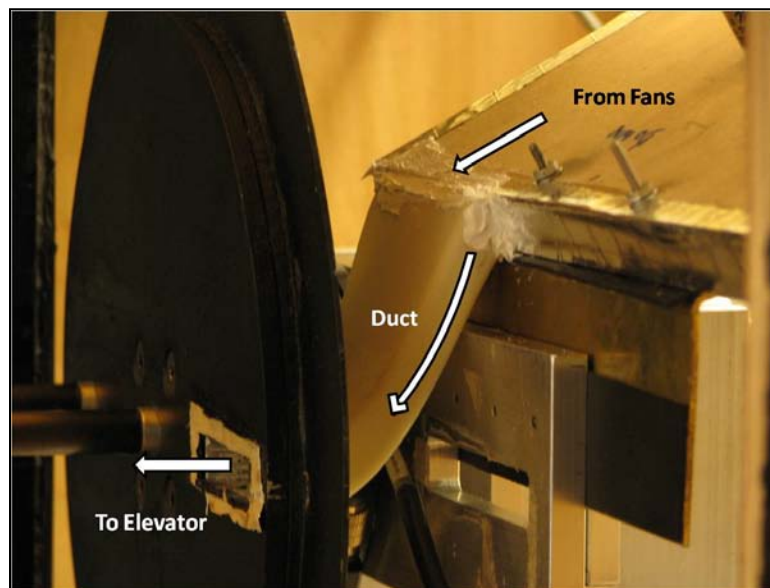


**Figure 50: View of the elevator mounting setup with the center section of wall removed**

## TEST MATRIX AND INFORMATION

Table 11 gives a summary of the tests conducted on the conventional and the active elevator.

**Table 11: Tests conducted in the wind tunnel**

<b>Elevator</b>	<b><math>V_{\infty}</math> (m/s)</b>	<b>AOA range</b>	<b>Configurations / Deflections</b>
Conventional	20	-5° through 14°	0°, 2.5°, -2.5°, 5°, -5°
Active	20	-8° through 14°	0°; Gurney flap at 45°,-45°;Jet flap at 45°, -45° at 10,000 rpm ( $ELC_{\mu}=0.0067$ ) and 14,000 rpm

The performance tests have been carried out at about 20 m/s yielding a Reynolds number of around  $3.785 \times 10^5$ . The actual dynamic pressures and angle of attacks have been recorded real time and used in data reduction and plotting. Data are typically recorded at 2° intervals except close to 0° and in the region of the maximum lift coefficient (9° to 14°), where 1° interval was used. The tests are run at two speeds of fans: 10,000 rpm ( $ELC_{\mu} = 0.067$ ) and 14,000 rpm.

## WIND TUNNEL TEST RESULTS

### Coefficient of Lift

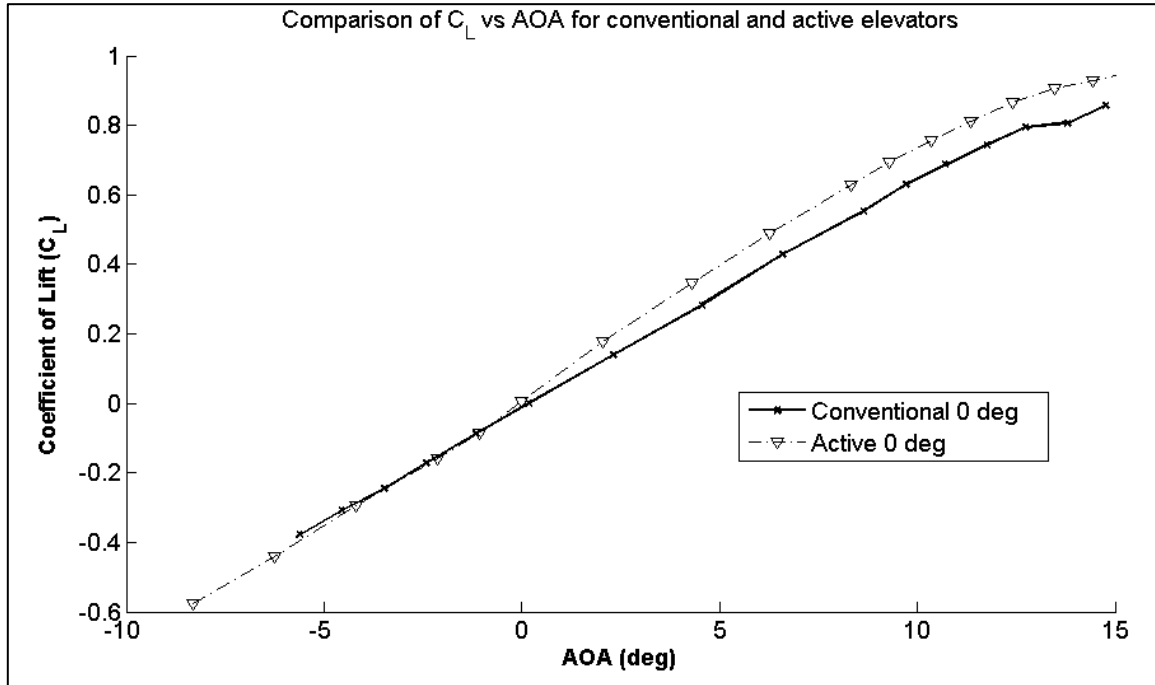


Figure 51:  $C_L$  Vs AOA for baseline configurations of conventional and active elevator

The  $C_L$  Vs AOA curves for  $0^\circ$  deflections of active and conventional elevators have been presented in Figure 51. The results indicate that the active elevator has greater slope. The difference in slope can be attributed to two factors. The active elevator has a slightly thicker airfoil (Figure 38) section and has cleaner top and bottom surface (Figure 34, Figure 35) as compared to the conventional elevator.

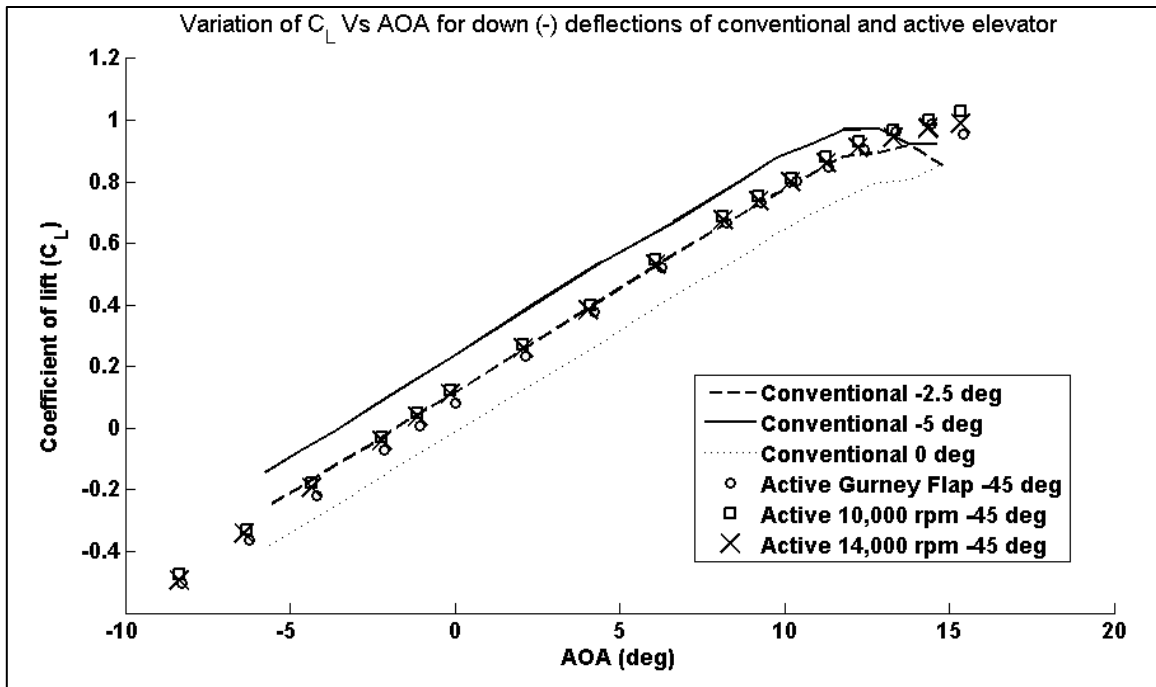


Figure 52:  $C_L$  Vs AOA for -ve (down) deflections of Conventional and active elevator

Figure 52 presents the  $C_L$  Vs AOA for active and conventional elevators for negative (downward) deflections. Figure 53 represents the plots for positive (up) deflections. There is an asymmetry in trends when the two plots are compared. For downward deflections, the amount of lift generated by the active elevator at 10,000 rpm and 14,000 rpm hovers around that generated by the conventional elevator at downward deflection of  $2.5^\circ$  while for upward deflection, the lift generated by the active elevator at 10,000 rpm is more than that generated by the conventional elevator at  $2.5^\circ$ . At 14,000 rpm compares to the lift generated at  $5^\circ$  deflection.

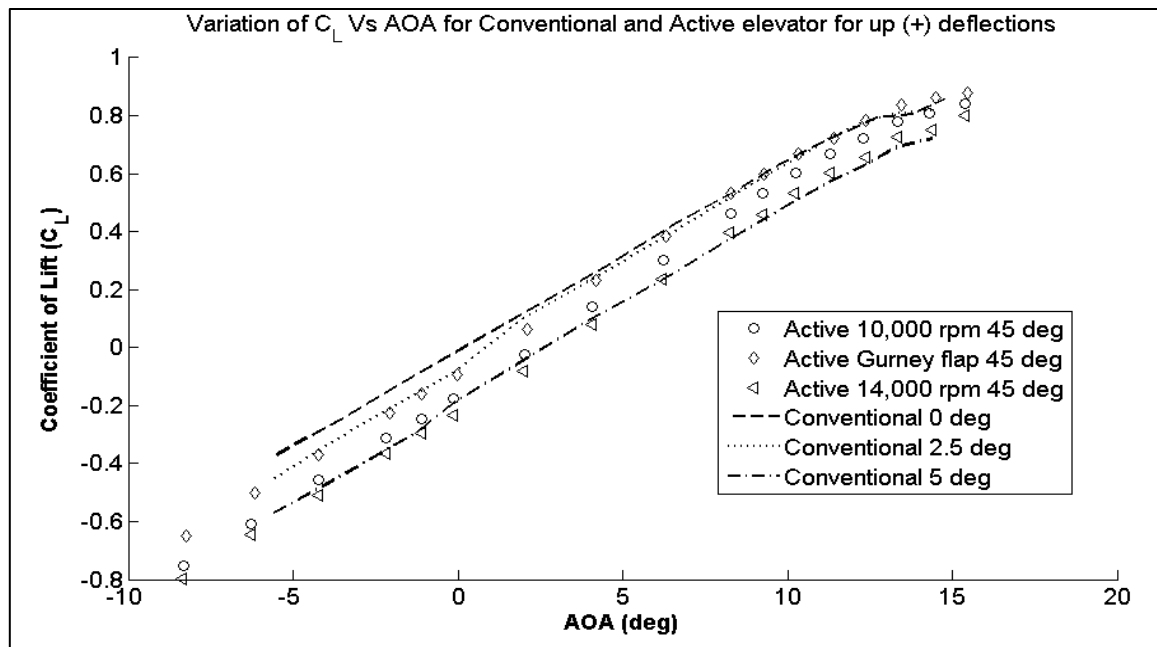


Figure 53:  $C_L$  Vs AOA for +ve (up) deflections of Conventional and active elevator

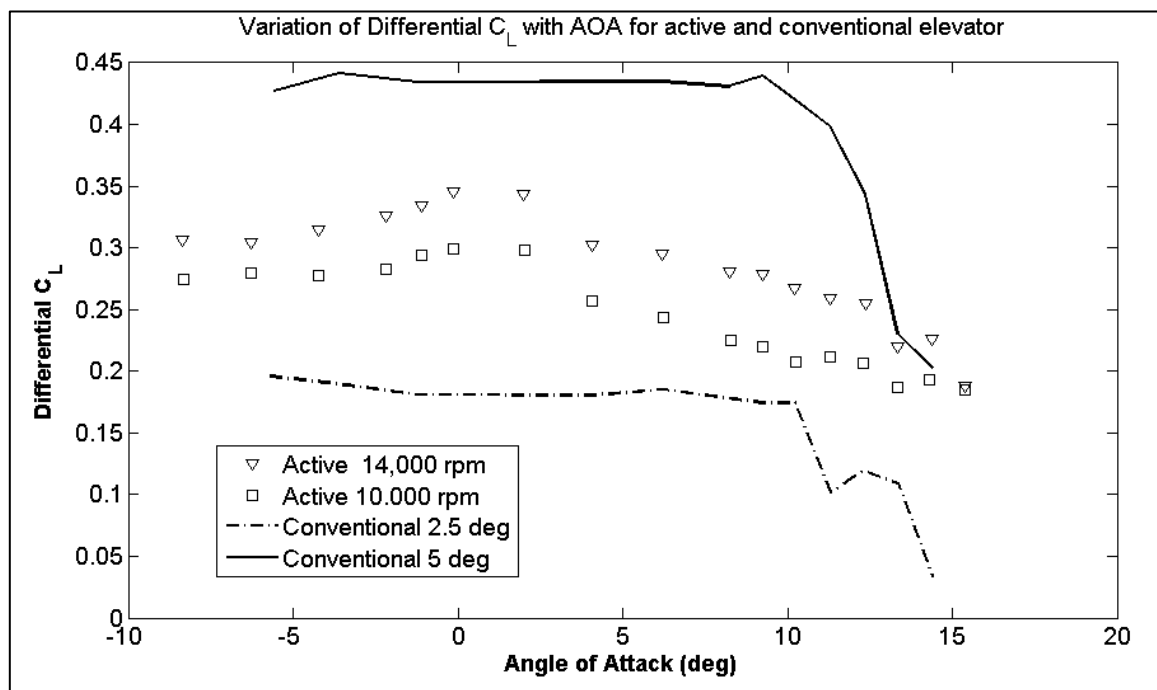


Figure 54: Differential  $C_L$  Vs. AOA for conventional and active elevators

This asymmetry is due to the imperfect manufacturing of the active elevator. It is likely that the deflection of jet flap on the active elevator is not symmetric about the chord line.

To facilitate comparison, a Differential Lift at an AOA has been defined as absolute difference of  $C_L$  values for positive and negative deflections of the control surface/ jet flap. It can also be interpreted as the amount of effectiveness of the elevator if it is deflected from a negative angle to same value of positive angle. For example, differential lift for  $2.5^\circ$  is the difference of  $C_L$  for  $-2.5^\circ$  defection and  $+2.5^\circ$  deflection. The results are plotted in Figure 54. The amount of differential lift for both 10,000 rpm and 14,000 rpm configurations of active elevator lie between  $2.5^\circ$  deflection and  $5^\circ$  deflection for conventional elevator. The differential lift for 14,000 rpm is higher than that for 10,000 rpm. The plots also suggest that at angles above  $10^\circ$ , the effectiveness of conventional elevator falls rapidly as the differential lift is seen to fall rapidly. On the other hand, the effectiveness of active elevator peaks at  $0^\circ$  AOA and falls gradually thereafter.

### **Coefficient of Drag**

The comparison between the coefficients of drag for negative deflections of the active and conventional elevators has been presented in Figure 55. The drag values for the active elevator are considerably higher. Also the drag values for the conventional elevator at all deflections remain lower than those for  $0^\circ$  deflection of the active elevator. The possible explanation for such a result requires a close look at the airfoil profiles shown in Figure 38. The active airfoil does not have a sharp trailing edge. This accounts

for a lot of the extra drag when compared to the conventional airfoil. Also, the higher thickness of the active elevator accounts for some extra drag. The drag values continue to increase as one moves to gurney flap, jet flap at 10,000 rpm and at 14,000 rpm as expected.

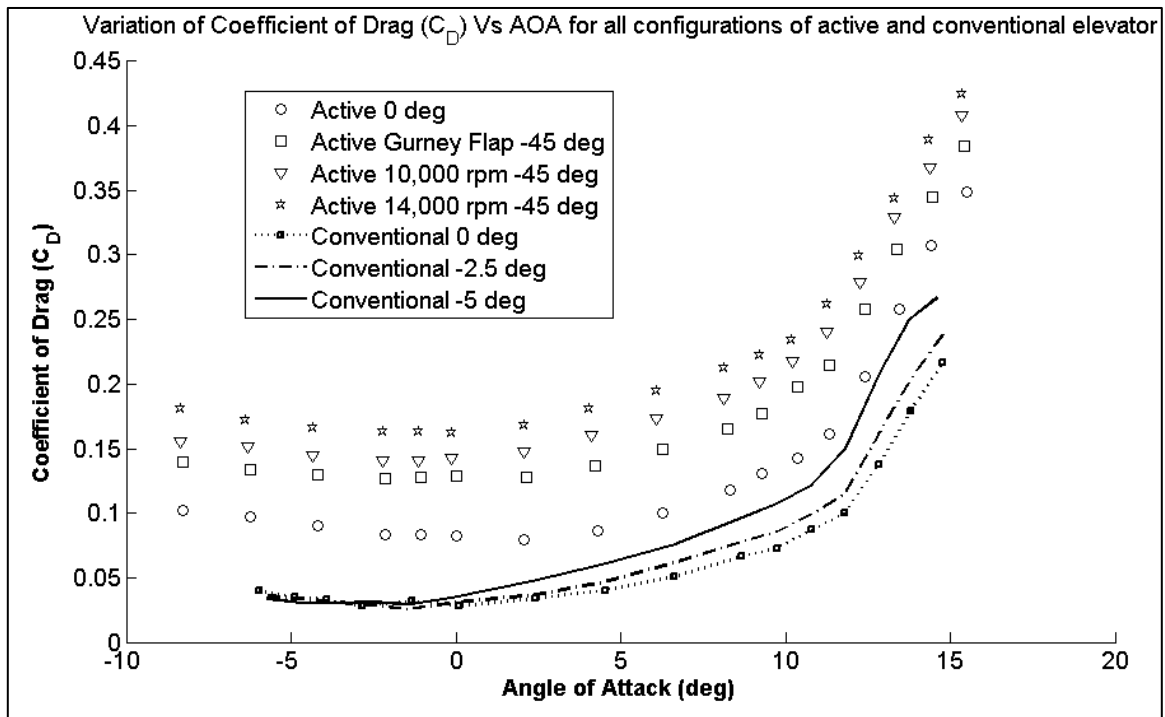


Figure 55:  $C_D$  Vs AOA for -ve (down) deflections of conventional and active elevator

Table 12 presents the uncertainty information for quantities pertaining to the measurement in 3'×4' wind tunnel.

**Table 12: Uncertainty information for elevator tests in 3'×4' wind tunnel**

Uncertainty in force measurement	2% of maximum value
Uncertainty in jet velocity, $V_{jet}$ measurement	0.52% of maximum value
Uncertainty in dynamic pressure measurement	0.1% of maximum value
Uncertainty in AOA measurement	0.25°

## **CHAPTER VI**

### **FLIGHT TESTING OF AIRCRAFT IN ROLL**

Flight testing of the aircraft is the concluding aspect of the project which completes the demonstration of transfer of lab tested technology to flight showing that active flow control based actuators can conventional ailerons. Flight testing of the aircraft with TE actuators is completed demonstrating roll control authority in banked turns.

#### **FLIGHT TEST PROCEDURE AND LOCATION**

Flight testing was carried out at Riverside Campus at Texas A&M University. Figure 56 shows a map of the riverside campus runways which were used for flying. The blue strip on the N-S runway is the approximate runway needed to take off. The yellow box represents the termination boundary. Four observers are placed at the four corners of the yellow box and in constant touch with the test director at the Ground Station in case the aircraft is observed to be out of the bounds. If the aircraft goes out of control, it can be manually killed and be contained inside the red box boundary which is the ultimate hazard footprint of the aircraft. Note that there are two locations for ground station on the map, one for morning and evening each. These are separated because the pilot, who stands near the ground station, preferred to always have the sun on his back while flying.

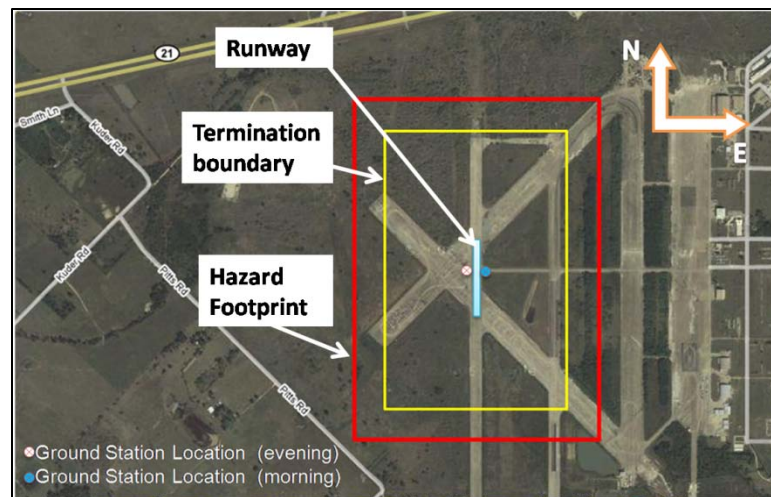


**Figure 56: Map of Riverside campus Runway**

## TESTED CONFIGURATIONS

Below are the definitions of various wings and ailerons involved in various tested configurations.

### *Original wings*

These wings are a part of the kit; also referred as the conventional wings.

### *Active wings*

Original Wings have been modified to fit the fluidic actuators

### *Heavy wings*

These wings are representative of the active wings in terms of mass distribution.

They are mock ups of active wings.

### *Full span ailerons*

The Original Wings on the aircraft are full span and thus are called Full Span

Ailerons

### *Reduced ailerons*

The inboard ailerons on heavy wings and active wings when used alone are called Reduced Ailerons

Table 13 shows the configurations tested in the flight test. They have been tested in the order mentioned in the table.

**Table 13: Tested configurations**

<b>Configuration</b>	<b>Wings</b>	<b>Actuators: Experimental Mode</b>	<b>Actuators: Safe Mode</b>
Baseline	Original Wings	Full Span Ailerons	Full Span Ailerons
Full Span	Heavy Wings	Full Span Ailerons	Full Span Ailerons
Reduced	Heavy Wings	Reduced Ailerons	Full Span Ailerons
Active Safe	Active wings	Reduced Ailerons	Reduced Ailerons
Active	Active wings	TE actuators	Reduced Ailerons

Flight test results are measured and modeled using Observer Kalman Filter Identification (OKID) analysis as explained in [33] to generate a dynamic model of the aircraft . This thesis presents flight tests for only two configurations namely, Full Span and Active. In Active configuration, take off and landing were performed with conventional ailerons to avoid risk of losing the aircraft. After takeoff, the control was switched to Jet Flaps and the motors were activated .The aircraft was trimmed controlled and banked for turns using TE actuators. During landing, the control was restored back to conventional ailerons.

## COMPARISON OF ROLL RATES AND ROLL ANGLES

Table 14 presents the comparison of roll angles and roll rates among the two configurations.

**Table 14: Comparison of roll rates and roll angles from OKID analysis**

Configuration	Run Number	Roll Rate	Roll Angle
<b>Full Span</b>	1	1.37	1.23
	2	1.38	1.24
	<b>Average</b>	<b>1.375</b>	<b>1.235</b>
<b>Active</b>	1	1.0	0.22
	2	1.2	0.40
	<b>Average</b>	<b>1.1</b>	<b>0.31</b>

The numbers (non-dimensional) in Table 14 are only representative of the roll angles and the roll rates. Figure 57 shows the roll rate with time from the flight data. It can be noted that for a step input in aileron deflection, the maximum roll rate is recorded to be around 130 °/s. Figure 58 shows the roll rate for a step input in control input to the jet flaps. In this case, the roll rate is limited to a maximum of 40°/s.

The pilot reported that changes in roll felt slower in Active Configuration compared to Full Span configuration but expressed confidence in control authority of TE actuators after getting a couple of flights in the Active configuration.

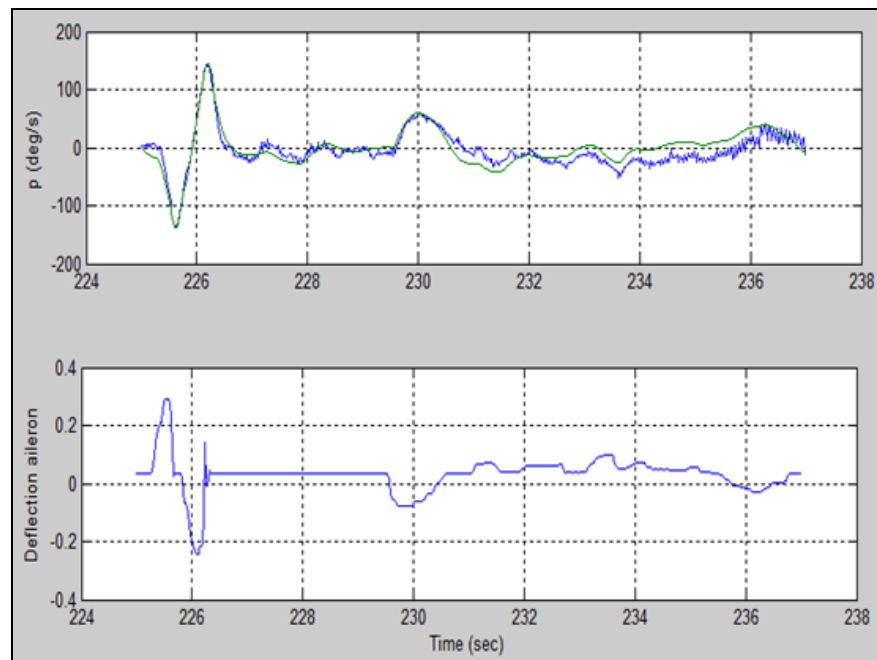


**Figure 57: Roll Rate for Full Span Configuration**

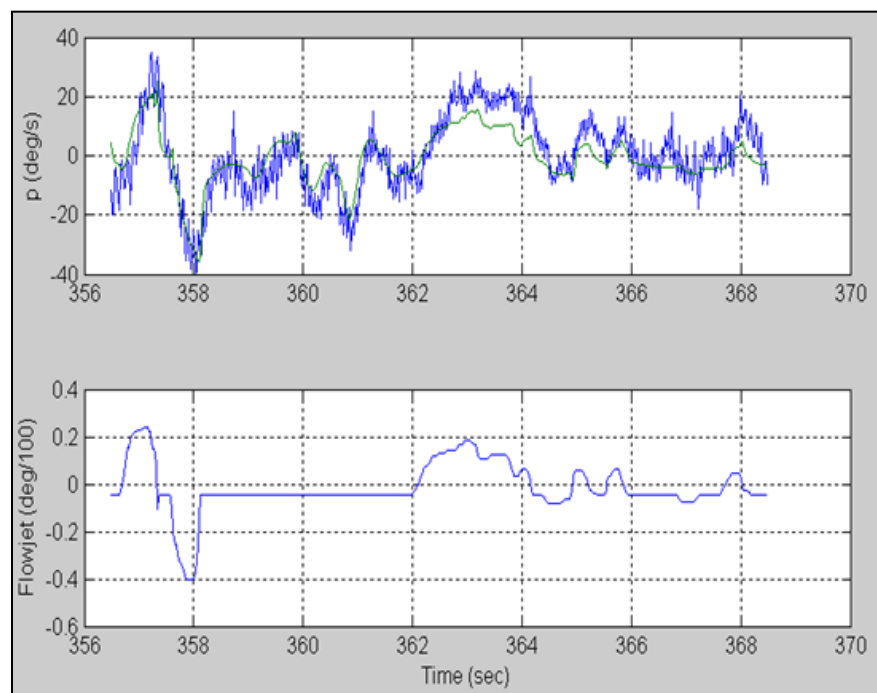


**Figure 58: Roll Rate for Active Configuration**

## **COMPARISON OF FLIGHT TESTS AND WIND TUNNEL RESULTS**

Wind tunnel tests indicate the TE actuators to be about 50 % as effective as the reduced ailerons and 25% as effective as the full span ailerons.

Flight tests data also indicates similar numbers. The roll rates as observed from Figure 57 and Figure 58 show that the TE actuators are less effective as compared to full span ailerons.

## **CHAPTER VII**

### **CONCLUSIONS**

The current work is the concluding effort of Phase II of the project titled UAV Hinge-less Flight Controls via Active Flow Control.

Continuing the effort from previous studies and construction, wind tunnel data for full scale testing of the 33% Extra 330S aircraft has been analyzed and findings indicate that the fluidic actuators have substantial effectiveness which has been measured to be roughly half the effectiveness of the reduced ailerons. Also observed is the effect of pulsed blowing in delaying the stall to at least  $22^\circ$  and pushing the maximum lift coefficient further. Synergy is also observed in LE pulsed blowing and TE continuous blowing when the TE jets are deflected down simultaneously in combination with LE actuators.

Pitch control using a similar TE fluidic actuator has been demonstrated. The design of an in-flight system to generate energized air is described. A similar system has been devised for a wind tunnel test and performance of the active elevator has been compared to a conventional elevator. Results indicate that the active elevator is as effective as the conventional elevator deflected at  $5^\circ$ . Finally, flight test results have been presented for roll control using TE actuators. The TE actuators were able to trim the aircraft and provide enough roll control authority to make successful turns without the use of conventional ailerons.

In all, active flow control technology in the form of continuous blowing has been demonstrated to replace conventional ailerons in flight. Wind tunnel studies indicate that pulsed blowing can be a promising technology in suppressing stall and operating at high AOA.

Future work can be pursued to implement active flow control based actuation for pitching and yawing. There is scope of improvement in increasing the uniformity in velocity profile across the span of trailing edge of the elevator.

## REFERENCES

1. Collis, S., Scott, Joslin, R. D., Seifert, A., and Theofilis, V., "Issues in Active Flow Control: Theory, Control, Simulation, and Experiment," *Progress in Aerospace Sciences*, Vol. 40, No.s 4-5, 2004, pp. 237-289.
2. Klausmeyer, S., Papadakis, M., and Lin, J., "A Flow Physics Study of Vortex Generators on a Multi-Element Airfoil," *AIAA Paper 96-0548*, Jan-1996.
3. Chang, R. C., Hsiao, F. B., and Shyu, R. N., "Forcing Level Effects of Internal Acoustic Excitation on the Improvement of Airfoil Performance," *Journal of Aircraft*, Vol. 29, No.5, 1992, pp. 823-829.
4. Huang, R. F., and Mao, S. W., "Separation Control on a Cantilever Wing with a Self-Excited Vibrating Rod," *Journal of Aircraft*, Vol. 39, No. 4, 2002, pp. 609-615.
5. Bechert, D. W., and Bartenwerfer, M., "The Viscous Flow on Surfaces with Longitudinal Ribs," *Journal of Fluid Mechanics*, Vol. 206, 1989, pp. 105-129.
6. Tillman, T.G., and Hwang, D.P., "Drag Reduction on a Large-Scale Nacelle Using a Micro-Blowing Technique," *AIAA-1999-130*, 37<sup>th</sup> Aerospace Sciences Meeting and Exhibit, Reno, NV, Jan. 11-14, 1999.
7. Regenscheit, B., "Drag Reduction by Suction of the Boundary Layer Separated Behind Shock Wave Formation at High Mach Number," *NACA-TM-1168*, 1947.

8. Modi, V. J., Munshi, S. R., Bandyopadhyay, G., and Yokomizo, T., "High-Performance Airfoil with Moving Surface Boundary-Layer Control," *Journal of Aircraft*, Vol. 35, No. 4, 1998, pp. 544-553.
9. Seifert, A., Bachar, T., Koss, D., Shepshelovich, M., and Wygnanski, I., "Oscillatory blowing: A Tool to Delay Boundary-Layer Separation," *AIAA Journal*, Vol. 31, No. 11, 1993, pp. 2052-60.
10. McManus, K., Ducharme, A., Goldey, C., and Magill, J., "Pulsed Jet Actuators for Suppressing Flow Separation," AIAA-1996-442, 34<sup>th</sup> Aerospace Sciences Meeting and Exhibit, Reno, NV, Jan. 15-18, 1996.
11. Hamdani, H., Nauman, M., and Parvez, K., "Separation Control by Alternating Tangential Blowing/Suction at Multiple Slots," *AIAA Journal*, Vol. 39, No. 4, pp. 735-737
12. Choi, K.S., and Clayton, B. R., "The Mechanism of Turbulent Drag Reduction with Wall Oscillation," *International Journal of Heat and Fluid Flow*, Vol. 22, 2001, pp. 1-9.
13. Ashpis, D. E., and Reshotko, E., "Vibrating Ribbon Problem Revisited," *Journal of Fluid Mechanics*, Vol. 213, 1990, pp. 531-547.
14. Amitay, M., and Glezer, A., "Aerodynamic Flow Control Using Synthetic Jet Actuators," AIAA-1998-208, 36<sup>th</sup> Aerospace Sciences Meeting and Exhibit, Reno, NV, Jan. 12-15, 1998.
15. Farnsworth, J. A. N., Vaccaro, J. C., and Amitay, M., "Active Flow Control at Low Angles of Attack: Stingray Unmanned Aerial Vehicle." AIAA-2007-4426,

- 25th AIAA Applied Aerodynamics Conference, Miami, Florida, June 25-28, 2007.
16. Gilarranz, J. L., Traub, L. W., and Rediniotis, O. K., "Characterization of a Compact, High-Power Synthetic Jet Actuator for Flow Separation Control," AIAA-2002-127, 40<sup>th</sup> AIAA Aerospace Sciences Meeting and Exhibit, Reno, NV, Jan. 14-17, 2002.
  17. Kähler, C. J., Scholz, P., Ortmanns, J., and Radespiel, R., "Towards Active Control of Leading Edge Stall by Means of Pneumatic Actuators," Active Flow Control: Papers contributed to the Conference "Active Flow Control 2006", Berlin, Germany, September 27 to 29, 2006, Springer Berlin, Vol. 95/2007, pp. 152-172
  18. Liebeck, R. H., "Design Of Subsonic Airfoils for High Lift," Journal of Aircraft, Vol. 15, No. 9, 1978, pp. 547-561.
  19. Neuhart, D., and Pendergraft, O., "A Water Tunnel Study of Gurney Flaps," NASA TM-4071, 1998.
  20. Myose, R., Heron, I., and Papadakis, M., "Effect of Gurney flaps on a NACA 0011 Airfoil," AIAA-1996-59, 34<sup>th</sup> Aerospace Sciences Meeting and Exhibit, Reno, NV, Jan. 15-18, 1996.
  21. Papadakis, M., Myose, R. Y., Heron, I., and Johnson, B. L., "An Experimental Investigation of Gurney Flaps on a GA(W)-2 Airfoil with 25 percent Slotted Flap," AIAA-1996-2437, AIAA Applied Aerodynamics Conference, 14th, New Orleans, LA, June 17-20, 1996.

22. Jeffrey, D., Zhang, X., and Hurst, D. W., "Aerodynamics of Gurney Flaps on a Single-Element High-Lift Wing," *Journal of Aircraft*, Vol. 37, No. 2, 2000, pp. 295-301.
23. Li, Y., Wang, J., and Zhang, P., "Influences of Mounting Angles and Locations on the Effects of Gurney Flaps," *Journal of Aircraft*, Vol. 40, No. 3, pp. 494-498.
24. Englar, R. J., "Circulation Control For High Lift And Drag Generation on STOL Aircraft," *Journal of Aircraft*, Vol. 12, 1975, pp. 457-463.
25. "Evaluation of Measurement Data - Guide to the expression of uncertainty in measurement," JCGM 100:2008, Joint Committee for Guides in metrology, 2008.
26. Traub, L. W., and Agarwal, G., "Exploratory Investigation of Geometry Effects on Gurney Flap Performance," *Journal of Aircraft*, Vol. 44, No. 1, 2007, pp. 349-351.
27. Traub, L. W., Miller, A. C., and Rediniotis, O., "Preliminary Parametric Study of Gurney-Flap Dependencies," *Journal of Aircraft*, Vol. 43, No. 4, 2006, pp. 1242-1244.
28. Traub, L. W., and Agarwal, G., "Aerodynamic Characteristics of a Gurney/Jet Flap at Low Reynolds Numbers," *Journal of Aircraft*, Vol. 45, No. 2, 2008, pp. 424-429.
29. Traub, L. W., Lund, D., Reeder, Z., and Rediniotis, O., "Preliminary Flight Tests of a Hinge-Less Roll Control Effector," *Journal of Aircraft*, Vol. 43, No. 4, 2006, pp. 1244-1246.

30. Agarwal, G., Rediniotis, O. K., and Traub, L. W., "An Experimental Investigation on the Effects of Pulsed Air Blowing Separation Control on NACA 0015," AIAA-2008-737, 46th AIAA Aerospace Sciences Meeting and Exhibit, Reno, Nevada, Jan. 7-10, 2008.
31. Agarwal, G., "Application of Active Flow Control Technology in an Unmanned Aerial Vehicle," M.S. Thesis, Department of Mechanical Engineering, Texas A&M University, College Station, 2007.
32. Rae, W. H. J. R., and Pope, A., "Low-speed Wind Tunnel Testing," New York, Wiley Interscience, Vol. 545, 1984.
33. Valasek, J., and Chen, W., "Observer/Kalman filter identification for online system identification of aircraft," Journal of Guidance, Control, and Dynamics Vol. 26, No. 2, 2003, pp. 347-353.

## VITA

Name: Yogesh Babbar

Address: 3141 TAMU, H R Bright Bldg. Room 701, College Station TX 77843

Email: yogeshbabbar@tamu.edu

Education: M.S., Aerospace Engineering, Texas A&M University, 2010  
B.E., Aeronautical Engineering, Punjab Engineering College,  
Chandigarh, India, 2006